Macroelement Model for the Progressive-Collapse Analysis of Infilled Frames

Original
Macroelement Model for the Progressive-Collapse Analysis of Infilled Frames / Di Trapani, F.; Tomaselli, G.; Cavaleri, L.; Bertagnoli, G.. - In: JOURNAL OF STRUCTURAL ENGINEERING. - ISSN 0733-9445. - STAMPA. - 147:6(2021), pp. 1-19. [10.1061/(ASCE)ST.1943-541X.0003014]

Availability:
This version is available at: 11583/2904494 since: 2025-02-12T13:17:54Z

Publisher:
American Society of Civil Engineers (ASCE)

Published
DOI:10.1061/(ASCE)ST.1943-541X.0003014

Macro-element Model for the Progressive Collapse Analysis of Infilled Frames

Fabio Di Trapani[1], Giovanni Tomaselli[2], Liborio Cavaleri[3], Gabriele Bertagnoli[4]

Abstract: A new multi-strut macro-model for the analysis of the progressive collapse response of infilled reinforced concrete (RC) frames is presented in the paper. The model consists of three struts, two outer infinitely rigid and resistant struts and one inner fiber-section strut. The inclination of the struts as well as the stress-strain response are modulated by two parameters which are obtained by means of analytical correlations provided in the paper. The latter link the geometric and mechanical properties of an infilled frame to the geometric configuration and mechanical response of the equivalent strut model. This confers the model the capability to adapt to consider different collapse configurations. The analytical correlations are obtained from an experimental dataset of pushdown tests, enlarged with data from refined finite-element (FE) simulations. Validation tests are finally carried out comparing the model prediction with results of experimental and FE pushdown tests not considered for the definition of the empirical database. Results show that, because of its flexibility, the model is sufficiently reliable and, at the same time, of simple implementation in FE analysis software to perform progressive collapse simulations.

Keywords: Progressive collapse, Robustness, Infilled frames, Reinforced concrete, OpenSees

[1]*Assistant Professor, Dipartimento di Ingegneria Strutturale, Edile e Geotecnica, Politecnico di Torino, Corso Duca degli Abruzzi 24, 10121 Torino, Italy (corresponding author). Email: fabio.ditrapani@polito.it.*

[2]*Postdoctoral Researcher, Dipartimento di Ingegneria Strutturale, Edile e Geotecnica, Politecnico di Torino, Corso Duca degli Abruzzi 24, 10121 Torino, Italy. Email: giovanni.tomaselli@polito.it*

[3]*Associate Professor, Dipartimento di Ingegneria, Università degli Studi di Palermo, Viale delle Scienze, 90128, Palermo, Italy. Email: liborio.cavaleri@unipa.it.*

[4]*Assistant Professor, Dipartimento di Ingegneria Strutturale, Edile e Geotecnica, Politecnico di Torino, Corso Duca degli Abruzzi 24, 10121 Torino, Italy. Email: gabriele.bertagnoli@polito.it.*

Introduction

Progressive collapse analysis and robust design of structures and infrastructures are emerging as hot topics in the last years for both researchers and practitioners. This is not only highlighted by the recent increase of numerical and experimental studies, but also the general directions of the latest updates of most of the technical codes indicate robustness as a trait of new construction (**Marchand and Stevens, 2016, Adam et al., 2018**), following the basic principle of robustness-based design according to which, the effect of an accidental damage suffered by a structure, would not be disproportionate with respect to the cause that generated it. For what concerns reinforced concrete frame building structures, the most critical condition inducing progressive collapse is generally related to the loss of a base column due, for instance, to impacts or explosions. In these condition vertical loads, and the arising inertial forces, are rapidly redistributed to the adjacent structural elements, the damage mechanism involves the beams converging to the column, which develop a resisting mechanism evolving in three sequential steps: a) a flexural resistant mechanism; b) a post-cracking arching mechanism; c) a catenary mechanism, triggering a large displacements regime (**Izzuddin et al., 2008, Weng et al., 2017**). The damage evolution is accentuated by the effect of gravity inertial forces arising and can be stopped within one of these three phases only if adequate resistance supply is available to achieve a new equilibrium configuration. Otherwise, collapse of the spans above the collapsed column occurs, also undermining the overall stability. Several authors have carried out studies concerning theoretical and practical assessment of this kind of progressive collapse response for frame structures. Among these **Izzuddin et al. (2008)** and **Vlassis et al., 2008** provided an effective method for the simplified evaluation of dynamic load-displacement demand, through a pseudo-static approach based on the energy balance between internal and external work for the substructural levels involved in the collapse mechanism. More recently experimental tests were carried out on scaled size structural elements (**Ren et al., 2016**) and structures (**Xiao et al., 2015**). Other experimental studies, accompanied by numerical interpretations (**Yu and Tan (2013), Pham et al. (2015), Pham et al. (2017)** and **Weng et al. (2017)**) have investigated the fundamental geometrical and mechanical aspects influencing the progressive collapse response of RC structures, providing also effective modelling strategies. A comprehensive state of the art illustrating the latest advances on gravity-induced collapse modeling for reinforced concrete structures has been also provided by **Kunnath et al. (2018)**. The major findings of the aforementioned studies report that the ductility of the beam end cross-sections plays a prominent role on the activation capacity of the catenary mechanism, but also that this is conditioned by many other factors such as the horizontal constraint degree as well as the real capacity of elongation of steel.

On the other hand, more recent studies, have demonstrated from the experimental and numerical point of view that the gravity-induced progressive collapse mechanism of frame structures is significantly altered by the presence of masonry infills (**Farazman et al., 2013, Xavier et al., 2015, Shan et al., 2016, Qian et al., 2017, Li et al., 2019, Di Trapani et al 2020a**). Therefore, the interaction between frames and infills due to lateral loads, which has been widely investigated in the past by experimental quasi-static tests (e.g. **Mehrabi et al. 1996, Colangelo 2005, , Kakaletsis, Karayannis 2009, Calvi and Bolognini 2001, Morandi et al. 2018)** and numerical studies addressing micro-modelling (e.g. **Mehrabi et al. 1997, Stavridis and Shing 2010, Caliò & Pantò 2014)** and equivalent single or multi-strut macro modelling **(e.g. Panagiotakos and Fardis 1996, El-Dakhakhni et al. 2003, Crisafulli and Carr 2007, Furtado et al., 2015, Di Trapani et al. 2020b**) also occurs in the case of gravity-induced progressive collapse. This has noticeable impact to the overall resistance increase, accompanied by a less prominent post-peak response and reduced propension in developing the catenary mechanism under the large displacement regime in comparison with bare frames. As a secondary effect, the increase in strength is also associated with a stiffness increment, causing an increase of the dynamic amplification factor (**Di Trapani et al., 2020a**). Therefore, the infilled frame has more resistance but, at the same time, the dynamic load demand increases too.

These premises make evident that progressive collapse of infilled frames cannot be assessed properly without an adequate modeling of frame-infill interaction. In particular, a simplified modelling strategy comes out as fundamental need to effectively assess progressive collapse response of infilled frames, although available experimental tests are still limited. Also for this reason, the proposed simplified macro-modeling approaches are theoretically based (e.g. **Farazman et al., 2013**) or not entirely generalizable, being validated on single experiments (e.g. **Li et al., 2019**). In a recent paper, **Di Trapani et al. (2020a)**, proposed the idea of three-strut fiber-section model, highlighting the importance of defining the inclination of the eccentric struts as a function of the geometrical and mechanical properties of the infilled frame. Despite this, no specific rules were given to define the inclination of the struts, and the predictive capacity of the model was tested only with a limited number of reference specimen tests, although with promising results.

Within this background, the paper formalizes the definition of a three-strut macro-element model based on the observation of the collapse mechanism of available experimental tests and refined numerical simulations of one-storey and multi-storey infilled frames. The model is defined using the *OpenSees* (**McKenna et al., 2000**) software platform. The major novelty is the definition of two parameters modulating the inclination of the struts and the resistance provided by the infill to the overall response. These parameters are easily evaluated through the analytical correlations provided in the paper, which put in relation the geometrical and mechanical characteristics of an infilled frame, with the geometric configuration and mechanical response of the equivalent strut model. In this way, the proposed model, can adapt its geometry and the stress-strain response of the struts to each infilled frame arrangement, providing a specialized simulation of the collapse mechanism. The aforementioned analytical correlation laws are obtained from an empirical dataset, specifically built by merging experimental pushdown test results and results from pushdown test simulation made with a refined finite element model. The validation of the model is carried against additional pushdown tests not previously considered for the definition of the dataset. A practical application of the proposed procedure is finally proposed for a six-storey building.

Proposed macro-element model formulation

The prosed modelling approach is based on the experimental observations of the damage mechanisms activating in single-storey and multi-storey infilled frames subject to pushdown tests. The model is implemented in OpenSees and is based on the adoption of distributed plasticity fiber-section elements for the RC frame. The model is easily reproducible with any finite element analysis program handling fiber-section elements. The experimental tests by **Li et al (2019)** and **Qian and Li (2017)** and the numerical investigations by **Di Trapani et al. (2020a)**, have clearly evidenced the behaviour of an infilled frame under progressive collapse conditions (**Fig. 1a-1b**), basically showing that:

- masonry portions enclosed at the corners undergoing a reduction of the original 90° angle in proximity of beam-column joints receive a confining action from the frame and because of this, undamaged corner regions form;
- confined masonry corner regions behave as rigid parts, inducing a migration of the position of the plastic hinges towards the inner part of the beam. In multi-storey infilled frames this occurs following a more or less linear pattern (**Fig. 1b, 2b**), so that for the external corner regions, the major movement of the plastic hinge position is observed at the highest floor (while no migration is observed at the lowest floor). This condition is inverted in correspondence of the internal corner regions. A as consequence of this, for the beams having intermediate position plastic hinges form in a position that can be approximately determined by intercepting the beam axis with the line joining the hinges at the upper and the lower floors (**Fig. 1b**).
- masonry at central zones undergoes significant damage due to diagonal compression. This induces sliding of bed joints and diagonal crushing in some cases.

A consequent schematization of the damage framework expected for building undergoing column losses is shown in **Fig. 2** for one-storey infilled frame buildings (**Fig. 2a**) and multi-storey infilled frame buildings (**Fig. 2b**). The major difference between these cases is related to the compression fields (depicted in blue in **Fig. 2**). In fact, as already mentioned, the masonry confined by the frame is subjected to significant compression stresses making these parts of the infill working as compression struts. The latter have a unique slope which connects the positions of the plastic hinges forming at different places in the beams. This means that, in multi-storey infilled frames, the position of the plastic hinges depends on the storey level, while for the one-storey cases the damage configuration is fixed. The proposed model is conceived to reproduce the experimentally observed mechanical response of the single-storey and multi-storey infilled frames. The schematization of the model is proposed in **Fig. 3** for both the cases. The model is composed of 3 struts per each infilled frame. Struts S2 have infinite stiffness and strength and are used to effectively simulate the observed damage mechanism in which masonry at corners remains almost intact. The product $\alpha_b l_b$ (α_b<1) represents the position of the connection node of the beam with the S2 strut. This consequently defines the angle of inclination of the struts and the location where the plastic hinge will form along the length l_b because of the interaction with the infill. As it can be observed in **Fig. 3**, the distance $\alpha_b l_b$ is defined once, both for the one-storey and multi-storey configurations, therefore the S2 struts of each infilled frame are parallel. For the multi-storey case, the connection points of S2 struts with the intermediate floor beams are obtained as the intersections of the straight lines connecting the origin points with the distances $\alpha_b l_b$ at the top and bottom beams with the intermediate beams themselves. S2 struts at the different floors are therefore aligned. The parameter α_b has a key role to the overall response, as it modulates the net length of the beams when the plasticization of the frame occurs. Therefore, high values of α_b are associated with a major contribution of the frame to the overall strength, while on the contrary, low α_b values induce minor frame resistance. More generally, the coefficient α_b considers the degree of coupling between the infill and the frame and therefore it defines the actual influence of the infill to the overall response of the frame. The definition of α_b is therefore of crucial importance as it defines the geometry of the entire resisting mechanism (**Fig. 3**) although its definition depends on a quite large number of factors as it will be described in the subsequent sections.

The S1 strut models the shear behaviour of the infill in the inner part, which is subjected to diagonal compression forces. The identification of S1 strut cross-section dimensions is performed starting from the procedure proposed by **Di Trapani et al. (2018)** as modified in **Di Trapani et al. (2020a)**. The thickness of the struts (t) is the same as the actual thickness of the infill, the equivalent strut width (w) is evaluated as:

$$w = \frac{h_c}{l_b} \frac{c^*}{\lambda^{*\beta^*}} d \tag{1}$$

where, with respect to the original formulation, the effect of vertical loads on columns is ignored in **Eq. (1)**, while the parameter λ^* is evaluated by means of the formula initially proposed by **Papia et al. (2003),** where the positions of l_b and h_b are inverted:

$$\lambda^* = \frac{\tilde{E}_m}{E_c} \frac{t l_b^{'}}{A_b} \left(\frac{l_b^{'2}}{h_c^{'2}} + \frac{1}{4} \frac{A_b}{A_c} \frac{h_c^{'}}{l_b^{'}} \right) \tag{2}$$

The symbols A_b and A_c represent the area of the cross-sections of beams and columns, E_c is the elastic modulus of the concrete frame, $\tilde{E}_m$ is the conventional elastic modulus taking into account both the Young's moduli of masonry along the two orthogonal directions (E_{m1} and E_{m2}) as:

$$\tilde{E}_m = \sqrt{E_{m1} \cdot E_{m2}} \tag{3}$$

while the other symbols are deducible from **Fig. 3**. Parameters c^* and β^* are evaluated by the following equations:

$$\begin{aligned} c^* &= 0.249 - 0.0116\nu + 0.567\nu^2 \cong 0.254 \\ \beta^* &= 0.146 - 0.0073\nu + 0.126\nu^2 \cong 0.147 \end{aligned} \tag{4}$$

depending on Poisson's ratio (ν) of the infill along the diagonal direction. For the sake of simplicity, the average Poisson's ratio can be used, otherwise the value ν=0.1 is assumed, providing the values resulting in **Eq. (4)**. S1 struts are no-tension inelastic fiber-section trusses modelled with a *Concrete02* material (parabolic with linear softening) available in *OpenSees*, defined by the four parameters $\tilde{f}_{md0}$ (peak-strength), $\tilde{f}_{mdu}$ (ultimate-strength), ε_{md0} (peak-strain), ε_{mdu} (ultimate strain)

(**Fig. 4a**). The equivalent strut is a phenomenological model which summarizes the complex response of the infill as a function of the boundary condition (e.g. aspect ratio, masonry orthotropy, influence of vertical stresses, frame-infill relative strength and stiffness). Therefore, the uniaxial stress-strain response of S1 strut will not be coincident to the masonry nominal one but will be related to it by the empirical relationships provided by **Di Trapani et al. (2018)**:

$$f_{md0} = \tilde{f}_m \cdot 26.9 \cdot \alpha^{-0.28} \tag{5}$$

$$f_{mdu} = f_{md0} \cdot (0.043 \cdot \beta - 0.06) \tag{6}$$

$$\varepsilon_{md0} = \varepsilon_{m0} \cdot 3.024 \cdot \gamma^{0.347} \tag{7}$$

$$\varepsilon_{mdu} = \varepsilon_{md0} \cdot 0.0184 \cdot \delta^{-1.166} \tag{8}$$

where, neglecting the influence of vertical loads on columns, and inverting the position of l_b and h_b, parameters α, β, γ and δ have the expressions:

$$\alpha = \frac{\tilde{f}_m^{\,2} \cdot w \cdot t}{f_{vm}^{\,0.2} \left(h_c / l_b\right) \cdot \lambda^{*0.2}} \tag{9}$$

$$\beta = \frac{f_{md0}^{\,0.7} \cdot w \cdot t}{\tilde{E}_m^{\,0.2} d} \tag{10}$$

$$\gamma = \left(\frac{f_{mdu}^{\,2}}{f_{md0}}\right)\left(\frac{E_c}{\tilde{E}_m^{\,1.5}}\right) \tag{11}$$

$$\delta = \tilde{E}_m^{\,0.20} \cdot \varepsilon_{md0} \tag{12}$$

in which it is conventionally assumed ε_{m0} = 0.0015 and $\tilde{f}_m = \sqrt{f_{m1} \cdot f_{m2}}$, is the conventional strength of the masonry, which takes into account the strengths along the two orthogonal directions (f_{m1} and f_{m2}). The peak and ultimate stresses $\tilde{f}_{md0}$ and $\tilde{f}_{mdu}$ are related with f_{md0} and f_{mdu} by a strength reduction coefficient ξ (≤1) taking into account a potential strength reduction associated with the different expected failure modes for the infilled frame subjected to vertical loads (instead of horizontal), as a function of the possible combination of geometric and mechanical characteristics of the infilled-frame system, therefore :

$$\tilde{f}_{md0} = \xi \cdot f_{md0}$$
$$\tilde{f}_{mdu} = \xi \cdot f_{mdu} \qquad (13)$$

The peak and ultimate strains are instead assumed as those evaluated by **Eqs. (7-8)** respectively.

Considering the above listed equations, the equivalent strut model is defined based on the two parameters α_b and ξ. Given the relevance that they assume on the overall response and the multitude of variables on which they the depend, the definition of α_b and ξ is carried out using an empirical approach rather than a mechanics-based one as described in the subsequent section.

As regards the reinforced concrete frame, this is modelled using distributed plasticity fiber-section elements. A *Concrete02* model is used for confined core and unconfined cover concrete fibers (**Fig. 4b**). Confined (f_{cc0}, f_{ccu}, ε_{cc0}, ε_{ccu}) and unconfined (f_{c0}, f_{cu}, ε_{c0}, ε_{cu}) concrete parameters are evaluated according to the model by **Razvi and Saatcoglu (1992)**. As regards rebars, given the large displacements and damage achieved by the frame during the pushdown analyses, it was necessary to include advanced material damage state. Rebars were modelled using the *Hysteretic* material backbone curve in order to simulate fracture in tension, in correspondence of the ultimate stress-strain capacity point (f_t, ε_{su}), and buckling in compression (if any) in correspondence of the stress-strain buckling point (σ^*,ε^*) evaluated according to the **Dhakal and Maekawa (2002)** model. Finally, the beam-columns intersection zones are modelled with rigid links. The definition of the rigid link extensions can be alternatively carried out using ASCE/SEI 41-17 provisions.

Framework and data-set for the empirical evaluation of coefficients α_b and ξ

The determination of parameters α_b and ξ is not easy to perform using a mechanical approach, in fact this would require strong assumptions about specific collapse modes for the frame-infill system, which are not simple to predict a-priori. The major unknown regards the masonry infill failure mode which can alternatively be due to mortar joints sliding, diagonal cracking or mixed modes, and that depends each time on the different combination of frame and infill mechanical and geometrical properties and lateral constraint conditions. The procedure here followed, provides instead the definition of two empirical correlations between the parameters α_b and ξ and the geometrical and mechanical characteristics of the frame-infill system.

In order to derive the analytical correlation, a dataset of reference experimental and numerical pushdown tests has been defined. The tests were simulated in *OpenSees* using the proposed equivalent strut model. Parameters α_b and ξ were initially assigned as trial values. The simulations were then repeated by iterating these parameter values up to the achievement of the best matching with the reference pushdown responses. The finally obtained values for α_b and ξ parameters were then stored and associated with the geometrical and mechanical data of the respective infilled frame. The procedure was repeated for all the reference tests. Since the availability of experimental tests is limited, the robustness of the data-set was increased using the also the results from refined finite element simulations of pushdown tests carried out by **Di Trapani et al. 2020a**. The steps of the framework are below summarized:

1. Acquisition of experimental test data (geometric and materials data, pushdown curves);
2. Modeling of each experimental test with the proposed multi-strut model;
3. Iterative calibration of parameters α_b and ξ;
4. Acquisition of numerical test data from a refined, experimentally validated, FE model;
5. Modeling of each experimental test with the proposed multi-strut model;
6. Iterative calibration of parameters α_b and ξ;
7. Definition of two analytical correlation laws between the obtained parameters α_b and ξ and the most representative geometrical and mechanical characteristics of the infilled frame;
8. Blind validation tests with experimental and FE specimens not included in the calibration phase.

A flow-chart of the framework is also illustrated in **Fig. 5**. The experimental tests used were those by **Qian and Li (2017)** (specimens WSS and WNL) and **Li et al. (2019)**. The formers are 1/4 scale two-storey reinforced concrete frames with brick masonry infills horizontally restrained from one-side only. The second is a 1/3 scale one-storey multi-bay reinforced concrete frames with brick masonry infills. The test set-up did not provide lateral constraints, but the frame had one bay at each side of the central bays involved in the pushdown tests.

The numerical specimens were those by **Di Trapani et al. (2020a)**. The latter are full scale one-storey one-bay infilled frames having different aspect-ratios, lateral constraint degree (free or fixed), beam cross-section aspect ratio and reinforcement arrangement (seismic or non-seismic). These specimens have been modelled in the Atena 2D Version 5 (**Cervenka et al. 2017**) software platform, which is based on a smeared cracking formulation for concrete and also supports frictional interfaces to be used for modeling mortar joints. The typical assembly of the FE model is illustrated in **Fig. 6a**. Concrete frame elements and masonry blocks are modeled by using CCIsoQuad nonlinear finite elements. The constitutive model associated with concrete elements and masonry units having a failure surface (**Fig. 6b**). Mortar joints are simulated using 2D interfaces governed by a Mohr-Coulomb failure surface depending on friction coefficient (μ) and cohesion (c) (**Fig. 6c**). The validation of the finite element modelling was performed by the authors in **Di Trapani et al. (2018)**. Details about the specimens and the test type are reported in **Table 1**. The identification the equivalent strut models is performed using **Eqs. (1-4)** for the determination of the S1 strut width and **Eqs. (5-12)** for the determination the nominal stress-strain response. Geometric and mechanical details of the experimental and numerical specimens together with the associated parameters identifying the equivalent struts are listed in **Tables 2-3**. Parameters α_b and ξ are assigned as trial values in the first step. Before starting the iterative calibration of α_b and ξ, the bare frame pushdown responses of the reference specimens and those provided by the models are compared. This preliminary comparison is carried out to check the reliability of the frame fiber-section model to reproduce the bare frame response, so that the subsequent calibration of parameters α_b and ξ will not be affected by a compensation of predictive errors of the frame model. For the sake of space only three sample comparisons between the bare frame reference specimens' responses and the bare frame model predictions are shown in **Figs. 7**. The latter confirm the reliability of the frame model in reproducing the pushdown tests.

Numerical simulation of the infilled frames pushdown tests is then carried out. Parameters calibration process is performed by comparing the reference pushdown responses and the model predictions iteratively varying parameters α_b and ξ to get the best matching of the curves. The basic matching criterion followed was an energetic criterion, that is the minimization of the difference between the areas below the reference pushdown curve of the specimen A_{exp} and the predicted one A_{pred}, so that $|A_{exp}\text{-} A_{pred}|$ is minimized. The adequacy of the results obtained by this approach was finally checked by the authors at the end of each test. The ranges of variation assumed were 0.15-0.5 for α_b and 0.25-1.0 for ξ. Results at the end of the calibration process are shown in **Fig. 8-9**, where numerical predictions and reference pushdown curves are depicted. It can be generally observed that, despite the large geometric and mechanical nonlinearity achieved during the tests, an adequate calibration of α_b and ξ allowed a sufficiently accurate prediction of the overall pushdown response, giving a positive feedback on the reliability of the proposed modelling approach. Some comparisons between the deformed shapes of the experimental and numerical specimens and those of the multi-strut models are shown in **Fig. 10**, demonstrating the consistency of the actual damage mechanisms with the predicted ones. Optimal results obtained for parameters α_b and ξ at the end of the calibration process of each specimen are finally listed in **Table 4**, together with the dimensional parameters resulting by their application. As regards α_b, the values range between 0.15 and 0.50, meaning that the plastic hinges in beams can form in a region comprised between 15% and 50% of the internal length l_b. This is definitely consistent with the experimental and numerical evidence from the considered specimens (**Fig. 10**). Regarding ξ values, the range is 25%-100% of the diagonal resistance f_{md0}. This wide range should not be surprising, but highlights the fact that the infill contribution to the overall resistance is extremely variable and depends on the resistance associated with the actual failure mechanism developing, as well described in the following section.

Empirical correlation laws for α_b and ξ

The experimental and numerical data-sets containing the calibrated parameters α_b and ξ together with the associated geometrical and mechanical features of the respective infilled frames are merged into a unique hybrid data-set. Results are then analyzed in order to understand the dependence of these parameters in a more general framework. An interpretation of the obtained α_b and ξ values can be given by recognizing the actual role of these parameters to the overall response. In fact, while ξ modulates the contribution of the infill in terms of strength, α_b modulates the shape of the collapse e mechanism, namely the amplitude of the intact portion of masonry enclosed at the corners. Consequently, α_b has effect on the vertical strength of the frame, as it defines the net shear span of the beams involved in the collapse mechanism (**Fig. 11**). The modulation by means of coefficients α_b and ξ allows considering the reciprocal influence of the frame to the final resistance of the infill and, vice versa, the influence of the infill to the final resisting mechanism of the frame. Consistently with this consideration, it can be observed the lowest ξ values are associated with specimens having reduced strength and stiffness of the frame with respect to that of the infill, so that a lower confining action is exerted and a sliding failure mode is more likely. On the contrary, a stronger confining action by a stiffer frame, will orient failure to a crushing mode which is typically associated with a larger strength. At the same time, the coefficient α_b has shown to be more influenced by the strength ratio between the frame and the infill, therefore the lower α_b values have been obtained for the frames having low strength with respect to the infill strength.

In this framework a crucial role is exerted by the lateral constraint degree, which influences the vertical stiffness of the frame and even more its strength. In fact, in the case of rigid or semi-rigid lateral contains, the axial force reaction to the pushing action of beams after the first cracking is relevant and significantly increases the resisting end moments (M_p^+, M_p^-). On the other hand, more effective lateral constraint degree increases the frame stiffness and the associated confining action to the infill with major exploitation of the infill strength. The scheme of the typical collapse mechanism is depicted in **Fig. 11** for the one-storey infilled frame.

Based on the aforementioned assumptions, the best correlation between ξ and the geometric and mechanical propertied of the frame-infill system is found with the parameter κ so defined:

$$\kappa = \frac{K_f}{K_s}\sqrt{\frac{l_b}{h_c}}\sqrt{\frac{\tilde{f}_m}{f_{vm}}} \tag{14}$$

where K_f is the conventional vertical stiffness of the frame obtained as the sum of the shear stiffnesses of the n_b beams involved in the mechanism:

$$K_f = \sum_{i=1}^{n_b} \psi_i \cdot \frac{E_{ci} I_{bi}}{l_{bi}^3} \tag{15}$$

and K_s is the conventional vertical stiffness contribution provided by the n_s infills involved in the mechanism at all the stories:

$$K_s = \sum_{j=1}^{n_s} \lambda_j \frac{\tilde{E}_{mj} \cdot t_j \cdot w_j}{d_j} \cdot \sin\theta_j \tag{16}$$

In the previous equation $i=1\ldots n_b$ is an index referred to the generic beam and $j=1\ldots n_s$ is an index referred to the generic strut. The coefficients ψ_i and λ_j are used consider the influence of the lateral constraint degree on the real stiffness of the beams and of the struts. The following boundary values are assumed depending on the type of constraint:

$$\psi_i = \begin{cases} 12 & \text{(rigid)} \\ 6 & \text{(free)} \end{cases} \qquad \lambda_j = \begin{cases} 1 & \text{(rigid)} \\ 0.5 & \text{(free)} \end{cases} \tag{17}$$

In **Eq. (16)**, θ_j is the angle of inclination of the S1 strut. For the one storey infilled frame this is depending only on the geometry of the frame, while in the case of a multi-storey infilled frame, this depending on α_b (**Fig. 3b**) which is still depending on θ_j. The determination of θ_j can be thus performed iteratively, or in a simpler way, this can be assumed as the average between the maximum and minimum slopes (θ_{max} and θ_{min} respectively) resulting by assuming α_b =0.5 and α_b =0.15 (**Fig. 12**):

$$\theta_j = \frac{\theta_{max} + \theta_{min}}{2} \quad (18)$$

where supposing that all the stories have the same interstorey height (h_c'), it can be easily found:

$$\theta_{max} = \arctan\left(\frac{nh_c'}{nl_b' - (n-1)(0.5l_b + 0.5h_{wc})}\right); \theta_{min} = \arctan\left(\frac{nh_c'}{nl_b' - (n-1)(0.15l_b + 0.5h_{wc})}\right) \quad (19)$$

Resulting values of K_f, K_s and κ for the different specimens are reported in **Table 5**. The best correlation between ξ and κ, fitting experimental and numerical data can be established by the following exponential correlation law (**Fig. 13a**):

$$\xi = 0.212 \cdot e^{1.45\kappa} \; \left(R^2 = 0.89\right) \quad (20)$$

which results in a determination coefficient of 0.89. The values of ξ resulting from **Eq. (20)** can be reasonably assumed in the range $0.25 \leq \xi \leq 1.0$.

The correlation of the parameter α_b with the characteristics of the infilled frame can be expressed as a function of the frame-infill strength ratio ρ, defined as:

$$\rho = \frac{R_f}{R_s} \quad (21)$$

in which R_f is the conventional vertical strength of the frame, obtained as:

$$R_f = \sum_{i=1}^{n_{M_p}} \frac{M_{p,i}^- + M_{p,i}^+}{l_b} \quad (22)$$

where, with reference to the simplified limit equilibrium scheme of the generic double span in **Fig. 14a**, the subscripts i denotes the generic plastic negative and positive moments at the ends of each beam involved in the collapse mechanism, n_{Mp} is the number of end cross-section where the plastic moments form, while l_b is the net span length. The plastic moments have positive sign and are evaluated considering the maximum axial forces acting on the beams during the pushdown analysis ($N_{b,max}$). R_s is the conventional vertical resistance provided by the infills, obtained considering the limit equilibrium of the hinged simplified scheme of the generic storey in **Fig. 14b** as:

$$R_s = \sum_{j=1}^{n_s} \tilde{f}_{mdo,j} \cdot t_j \cdot w_j \cdot \sin\theta_j \quad (23)$$

where the subscript j denotes the terms related to the generic S1 strut involved in the collapse mechanism. For the correlation between ρ and α_b two possible expressions are provided (**Fig. 13b**):

$$\alpha_b = -0.09\rho^3 + 0.54\rho^2 - 1.05\rho + 0.86 \qquad (R^2 = 0.93) \quad (24)$$

$$\alpha_b = 0.28\rho^{-0.58} \qquad (R^2 = 0.87) \quad (25)$$

The two expressions have similar determination coefficients (0.93 and 0.87 respectively) and can be used alternatively or to get an average value for α_b . Consistently with the actual experimental and numerical observations, the values of ξ resulting from **Eqs. (24-25)** can assumed be in the range 0.15 $\leq \alpha_b \leq$ 0.5. Resulting values of R_f, R_s, ρ and $N_{b,max}$ for the different specimens are reported in **Table 5**. It is noteworthy observing that the determination of the strength of the frame (R_f), and therefore of the coefficient ρ, is subject to the evaluation plastic moments at the ends of the beams, which in turn are depending on the maximum axial forces ($N_{b,max}$) developing because of the pushing action of the beams on the lateral supports. The latter are not straightforward to evaluate in practice, since they vary at each step of the pushdown analysis, therefore, in order to use **Eq. (22)**, two strategies can be adopted. The first is running a pushdown analysis supposing a trial value of α_b to get an estimation of the maximum axial forces acting on beams. The second is using the analytical correlation laws defined as described in the following.

The maximum compression axial force achieved by the beams in a pushdown tests basically depends on two factors. One is the lateral constraint degree, the more the constraints are stiff, the more the axial lateral reaction increases and so the axial force. The second is the beam height-to-length ratio ($\chi = h_{wb}/l_b$), as this conditions to the arching action developed by the beams after the first cracking. This is clear from **Fig. 15a**, which shows the distribution of maximum dimensionless axial forces ($\nu_{b,max} = N_{b,max}$ / f_c b_{wb} h_{wb}) recorded for the previously analyzed experimental and numerical specimens as a function of χ and the lateral restraint conditions. In **Fig. 15b**, the trend of the average dimensionless axial forces in beams is reported as a function of the vertical displacement and for the different constraint conditions.

It is found that the two following simple polynomial correlation can be defined between $\nu_{b,max}$ and χ for the two cases of rigid and free lateral constraints:

$$\nu_{b,max} = \begin{cases} -8.27\chi^2 + 2.74\chi + 0.017 & \text{(rigid)} \\ -5.79\chi^2 + 1.36\chi - 0.041 & \text{(free and rigid-free)} \end{cases} \qquad (26)$$

As previously mentioned, expressions in **Eq. (25)** can be used as a simple way to predict the maximum axial force acting on the beams and therefore estimating the associated plastic moments to introduce in **Eq. (22)**. An interpolation between the two functions can be used to estimate $\nu_{b,max}$ the cases having semi-rigid connections.

Blind validation tests

Based on the obtained formulation, the procedure for the complete analytical definition of the proposed infilled frame multi-strut model follows the below reported steps:

1. Evaluation of the equivalent strut width w (**Eqs. 1-4**);
2. Evaluation of the nominal stress-strain parameters of S1 strut (f_{md0}, f_{mdu}, ε_{md0}, ε_{mdu}) (**Eqs. 5-12**);
3. Determination of ξ (**Eqs. 14-20**);
4. Determination of $\tilde{f}_{md0}$ and $\tilde{f}_{mdu}$ (**Eqs. 13**);
5. Determination of α_b (**Eqs. 21-26**);

This procedure has been validated by applying it for the simulation of four reference tests not belonging to previously defined data-set used to build the empirical correlations. The specimens consisted of one experimental test by **Qian and Li (2017)** (Specimen WNS) and three numerical tests of the refined FE models by **Di Trapani et al (2020a)** Details about the specimens and the test types are reported in **Table 6**, while **Tables 7-8** collect all the fundamental geometric and mechanical data for the definition of the equivalent strut and the nominal stress-strain parameters. Parameters κ and

ρ, evaluated according to **Eqs. (14)** and **(21)** are reported in **Table 9**, together with the dimensionless axial forces ($\nu_{b,max}$) estimated by **Eq. (26)**. Parameters α_b and ξ finally resulting are reported in **Table 10**. The comparison between experimental force-displacement curves and numerical predictions are depicted in **Fig. 16**. It can be observed that for all the considered cases, numerical predictions resulted in a very good agreement with the test data, providing a sufficiently reliable prediction of the peak resisting capacity and the post-peak branch, despite the large uncertainty associated with the advanced damage state of materials during the tests. This result is also confirmed by the consistency between actual and predicted deformed shapes as illustrated in **Fig. 17**.

Application of the proposed method to a case-study structure

The proposed modelling methodology is applied to perform the progressive collapse analysis of infilled frames case-study structure. A multi-bay, six-stories infilled frame reinforced concrete structure (**Fig. 18**) is used as example. The structure is supposed undergoing the central columns loss. The frame is constituted by concrete having compressive strength f_c=25 MPa and steel rebars with yielding stress f_y=450 MPa. The structure is designed according to the Italian design regulation (NTC 2018). Geometric and mechanical details of the frame and of the infills are reported in **Table 11**. Detail of reinforcement of the central spans are illustrated in **Table 12**. As regards the infills outside the progressive collapse mechanism, these are modelled with a standard equivalent strut model (e.g. **Di Trapani et al., 2018**). A semi-rigid lateral constrain degree is assumed for the first five stories, while for the last storey the constraint degree is supposed as free. The structure is subjected to a pushdown tests, comparing the results with those obtained supposing the bare frame configuration in the central bays. The detailed calculation steps are exposed in Appendix. The resulting geometry for the equivalent strut model is illustrated in **Fig. 19**.

Results of the pushdown tests are shown in **Fig. 20a**. The latter show a strength increment of +40% for the model having the infills in the central bays and noticeable stiffness increase. The post-peak behaviour is, as expected, characterized by a rapid strength loss associated with the failure of the infills. On the contrary, the model with bare central spans shows a more ductile behaviour up to a displacement of 200 mm followed by a rapid strength loss. The two models show similar residual resistance in the last stages of the test. A test of the adequacy of the hypothesis of considering a semi-rigid behaviour of lateral constrains by **Eq. (25)** has been also carried out. **Fig. 20b** shows a good agreement between the average maximum value of the dimensionless axial force predicted by **Eqs (25)** and the actual dimensionless axial force trend during the analysis. The deformed shapes at the same vertical displacement (300 mm) of the two models are finally shown in **Fig. 21**.

Conclusions

The simulation of progressive collapse response of frame structures due to accidental column losses is complicated because of the high mechanic and geometric nonlinearity. The complexity of the collapse mechanism is accentuated by the influence of masonry infills which significantly interact with primary RC structures. From the observation of experimental and numerical pushdown tests it is evident that the infill-frame interaction induce: a) a migration of the plastic hinges towards the inner part of the beams; b) the formation of regions without damage for the masonry portions enclosed at the corners because of the confining action exerted by the frame in the collapsed central column configuration; b) the sliding of bed-joints or diagonal crushing in the central zones of the infills. These mechanisms can influence in a more or less relevant way the overall resistance, and this depends each time on the coupling between the frame and the infill.

The paper presented a simplified multi-strut macro-model to be used for progressive collapse simulations. The major novelty is just the capability of the model to adapt its geometry and mechanical properties of the struts as a function the characteristics of the infilled frame, to match as much as possible the mechanisms above described. The model provides different definition of the geometry in the case of multi-storey frames. The definition of the model is regulated by two fundamental parameters, α_b and ξ, modulating the slope of the external struts and the stress-strain of the central strut respectively. These parameters can be evaluated by the analytical correlations provided in the paper and basically depend on the strength and stiffness ratios between the frame and the infill. The analytical correlations have been obtained from an empirical hybrid dataset, defined by merging test data from real experimental tests and refined numerical simulations. The validation of the model, carried out against four external blind tests, gave confirmation of a sufficient predictive reliability of the model, even in consideration of the significant uncertainties affecting the response of infilled frame systems. Concluding, the proposed model results a flexible and computationally effective instrument to be used for the design and the assessment of robustness of new and existing reinforced concrete infilled frames. Considering the noticeable influence of the infills to the overall progressive collapse response, future works could exploit this modelling methodology to investigate and compare the progressive collapse responses of bare and infilled frames under dynamic regime.

APPENDIX – Details of calculations for the sample structure

With reference to the geometric and material details reported in **Table 11** for the sample structure, the definition of the multi-strut model provides the following calculation steps:

1. Calculate $\lambda^*, c^*, \beta^*, w$ for S1 strut

$$\lambda^* = \frac{\tilde{E}_m}{E_c}\frac{t l_b^{'}}{A_b}\left(\frac{l_b^{'2}}{h_c^{'2}} + \frac{1}{4}\frac{A_b}{A_c}\frac{h_c^{'}}{l_b^{'}}\right) = \frac{5675}{31476}\frac{300\times 6300}{150000}\left(\frac{6300^2}{3400^2} + \frac{1}{4}\frac{150000}{320000}\frac{3400}{6300}\right) = 7.94 \qquad (27)$$

$$c^* \cong 0.254; \quad \beta^* \cong 0.147 \qquad (28)$$

$$w = \frac{h_c}{l_b}\frac{c^*}{\lambda^{*\beta^*}} d = \frac{2900}{5500}\frac{0.254}{7.94^{0.147}} 7159 = 707 mm \qquad (29)$$

2. Calculate the nominal stress-strain parameters for S1 strut $f_{md0}, f_{mdu}, \varepsilon_{md0}, \varepsilon_{mdu}$ (**Eqs. 5-12**);:

$$\alpha = \frac{\tilde{f}_m^{\,2}\cdot w \cdot t}{f_{vm}^{\;0.2}\left(h_c / l_b\right)\cdot \lambda^{*0.2}} = \frac{6.02^2 \times 707 \times 300}{1.07^{0.2}\left(2900/5500\right)7.94^{0.2}} = 9.50\times 10^6 \qquad (30)$$

$$\beta = \frac{f_{md0}^{\;\;0.7}\cdot w \cdot t}{\tilde{E}_m^{\;0.2} d} = \frac{1.61^{0.7}\times 707 \times 300}{5675^{0.2} 7159} = 7.34 \qquad (31)$$

$$\gamma = \left(\frac{f_{mdu}{}^{2}}{f_{md0}} \right) \left(\frac{E_c}{\tilde{E}_m{}^{1.5}} \right) = \left(\frac{0.41^2}{1.61} \right) \left(\frac{31476}{5675^{1.5}} \right) = 0.00772 \tag{32}$$

$$\delta = \tilde{E}_m{}^{0.20} \cdot \varepsilon_{md0} = 5675^{0.20} \times 0.000839 = 0.00473 \tag{33}$$

$$f_{md0} = \tilde{f}_m \cdot 26.9 \cdot \alpha^{-0.287} = 6.02 \times 26.9 \times \left(9.50x10^6 \right)^{-0.287} = 1.61\text{MPa} \tag{34}$$

$$f_{mdu} = f_{md0}(0.043 \cdot \beta - 0.06) = 1.61(0.043 \times 7.34 - 0.06) = 0.41\text{MPa} \tag{35}$$

$$\varepsilon_{md0} = \varepsilon_{m0} \cdot 3.024 \cdot \gamma^{0.347} = 0.0015 \times 3.024 \times 0.00772^{0.347} = 0.000839 \tag{36}$$

$$\varepsilon_{mdu} = \varepsilon_{md0} \cdot 0.0184 \cdot \delta^{-1.166} = 0.000839 \cdot 0.0184 \cdot 0.00473^{-1.166} = 0.00794 \tag{37}$$

3. Calculate ξ (**Eqs. 14-20**)

$$\theta_{\min} = \arctan\left(\frac{nh_c^{'}}{nl_b^{'} - (n-1)(0.15l_b + 0.5h_{wc})} \right) = \\ = \arctan\left(\frac{5 \times 3400}{5 \times 6300 - 4(0.15 \times 5500 + 0.5 \times 800)} \right) = 32.6° \tag{38}$$

$$\theta_{\max} = \arctan\left(\frac{nh_c^{'}}{nl_b^{'} - (n-1)(0.5l_b + 0.5h_{wc})} \right) = \\ = \arctan\left(\frac{5 \times 3400}{5 \times 6300 - 4(0.5 \times 5500 + 0.5 \times 800)} \right) = 42.0° \tag{39}$$

$$\theta_j = \frac{\theta_{min} + \theta_{max}}{2} = \frac{32.6° + 42.0°}{2} = 37.3° \tag{40}$$

The beams belonging to the first five spans are considered having a semi-rigid lateral constrains at the ends (ψ_i=9, λ_j=0.75). The beams belonging to the last span are considered having no lateral constrains (ψ_i=6, λ_j=0.75). Therefore:

$$K_f = \sum_{i=1}^{n_b} \psi_i \cdot \frac{E_{ci} I_{bi}}{l_{bi}^3} = (9 \times 10 + 6 \times 2) \times \frac{31476 \times 3125000000}{5500^3} = 60303 kN/m \tag{41}$$

$$K_s = \sum_{j=1}^{n_s} \lambda_j \frac{\tilde{E}_{mj} \cdot t_j \cdot w_j}{d_j} \cdot sin\theta_j = (0.75 \times 8 + 0.5 \times 2) \times \frac{5675 \times 300 \times 707}{7159} \sin(37.3°) = 713208 kN/m \tag{42}$$

$$\kappa = \frac{K_f}{K_s} \sqrt{\frac{l_b}{h_b}} \sqrt{\frac{\tilde{f}_m}{f_{vm}}} = \frac{60303}{713208} \sqrt{\frac{5500}{2900}} \sqrt{\frac{6.02}{1.07}} = 0.28 \tag{43}$$

$$\xi = 0.212 \cdot e^{1.45\kappa} = 0.212 \cdot e^{1.45 \times 0.28} = 0.32 \tag{44}$$

4. Calculate $\tilde{f}_{md0}$ and $\tilde{f}_{mdu}$ (**Eqs. 13**):

$$\tilde{f}_{md0} = \xi \cdot f_{md0} = 0.32 \times 1.61 = 0.51 \text{ MPa} \tag{45}$$

$$\tilde{f}_{mdu} = \xi \cdot f_{mdu} = 0.32 \times 0.41 = 0.13 \text{ MPa} \tag{46}$$

5. Calculate α_b (**Eqs. 21-26**):

$$\chi = \frac{h_{wb}}{l_b} = \frac{500}{5500} = 0.091 \tag{47}$$

Consistently with the previous assumptions the dimensionless axial forces of the beams belonging to the first five spans are evaluated as average ($\nu_{b,max(semi\text{-}rigid)}$) between the values obtained from the two expressions in **Eq. (26)**. The second expression in **Eq. (26)** is used for the top beams ($\nu_{b,max(free)}$).

$$\nu_{b,\max(rigid)} = -8.27\chi^2 + 2.74\chi + 0.02 = -8.27 \times 0.091^2 + 2.74 \times 0.091 + 0.02 = 0.20 \tag{48}$$

$$\nu_{b,\max(free)} = -5.79\chi^2 + 1.36\chi - 0.04 = -5.79 \times 0.091^2 + 1.36 \times 0.091 - 0.04 = 0.036 \tag{49}$$

$$\nu_{b,\max(\text{semi-rigid})} = \nu_{b,\max(\text{rigid})} + \nu_{b,\max(\text{free})} = \frac{0.20 + 0.036}{2} = 0.12 \tag{50}$$

The resulting axial forces used to evaluate the plastic end moments of the beams are then:

$$N_{b,\max(\text{semi-rigid})} = \nu_{b,\max(\text{semi-rigid})}\, f_c h_{wb} b_{wb} = 0.12 \times 25 \times 500 \times 300 = 450000\, N = 450 \text{ kN} \tag{51}$$

$$N_{b,\max(free)} = \nu_{b,\max(\text{free})}\, f_c h_{wb} b_{wb} = 0.036 \times 25 \times 500 \times 300 = 135000 N = 135 \text{ kN} \tag{52}$$

It follows:

$$R_f = \sum_{i=1}^{n_{M_p}} \frac{M_{p,i}^-}{l_b} + \sum_{i=1}^{n_{M_p}} \frac{M_{p,i}^+}{l_b} = 2\left(\frac{368.5 + 368.5 + 368.5 + 327.8 + 327.8 + 273.3}{5.5}\right) + 2\left(\frac{265.2 + 265.2 + 265.2 + 224.6 + 224.6 + 154.7}{5.5}\right) = 1249 \text{ kN} \tag{53}$$

$$R_s = \sum_{j=1}^{n_s} \tilde{f}_{mdo,j} \cdot t_j \cdot w_j \cdot \sin\theta_j = 10 \times 0.51 \times 300 \times 707 \times \sin(37.3°) = 655503 \text{ N} = 655.5 \text{ kN} \tag{54}$$

$$\rho = \frac{R_f}{R_s} = \frac{1249}{655.5} = 1.90 \tag{55}$$

Calculation of α_b using **Eq. (24)**

$$\alpha_b = -0.09\rho^3 + 0.54\rho^2 - 1.05\rho + 0.86 = -0.09\times1.90^3 + 0.54\times1.90^2 - 1.05\times1.90 + 0.86 = 0.20 \quad (56)$$

$$\alpha_b l_b = 0.20\times5500 = 1100 \text{ mm} \quad (57)$$

Alternative calculation of α_b using **Eq. (25)**

$$\alpha_b = 0.28\rho^{-0.58} = 0.28\cdot1.90^{-0.58} = 0.19 \quad (58)$$

Data Availability Statement

Some or all data, models, or code generated or used during the study are available from the corresponding author by request. (OpenSees models).

References

Adam, J.M., Parisi, F., Sagasetac, J., Lu, X. 2018. “Research and practice on progressive collapse and robustness of building structures in the 21st century.” *Eng. Struct*. 173: 122–149.

Caliò, I., Pantò, B. 2014. “A macro-element modelling approach of Infilled Frame Structures.” *Computers & Structures* 143:91–107.

Calvi, G.M., Bolognini, D. 2001. “Seismic response of reinforced concrete frames infilled with weakly reinforced masonry panels.” *J. Earthq. Eng.* 5(02):153–85.

Cervenka, J., L. Jendele, and V. Cervenka. 2017. ATENA program documentation. Praha 5, Czech Republic: Cervenka ConsultingColangelo, F. 2005 “Pseudo-dynamic seismic response of reinforced concrete frames infilled with non-structural brick masonry.” *Earthquake Eng Struct Dyn* 34: 1219–1241.

Crisafulli, F.J., Carr, A.J. 2007. “Proposed macro-model for the analysis of infilled frame structures.” *Bull N Z Soc Earth. Eng.* 40(2):69–77.

Dhakal, R.P., Maekawa, K. 2002. “Modeling for Postyield Buckling of Reinforcement.” *J. Struct. Eng.* 128(9): 1139-1147.

Di Trapani, F., Bertagnoli, G., Ferrotto, M.F., Gino, D. 2018. “Empirical equations for the direct definition of stress-strain laws for fiber-section based macro-modeling of infilled frames.” *J. Eng. Mech.* 144(11): 04018101.

Di Trapani, F., Giordano, L., Mancini, G. 2020-a. “Progressive Collapse Response of Reinforced Concrete Frame Structures with Masonry Infills.” *J. Eng. Mech.* 146(3): 04020002

Di Trapani F., Bolis V., Basone F., Preti M. 2020-b. “Seismic reliability and loss assessment of RC frame structures with traditional and innovative masonry infills.” *Eng. Struct.* 208:110306.

El-Dakhakhni, W., Elgaaly, M., Hamid, A. 2003. Three-Strut model for concrete masonry infilled steel frames. *J. Struct. Eng*. 129(2):177–85.

Farazman, S., Izzuddin, B.A, Cormie, D. 2013. “Influence of Unreinforced Masonry Infill Panels on the Robustness of Multistory Buildings.” *J. Perform. Constr. Facil*. 27(6): 673-682.

Furtado, A., Rodrigues, H., Arêde, A., Varum, H. 2015. “Simplified macro-model for infill masonry walls considering the out-of-plane behaviour.” *Earthquake engineering and structural dynamics* 45(4): 507-524.

Izzuddin, B.A., Vlassis, A. G., Elghaz1ouli, A. Y., Nethercot, D.A. 2008. “Progressive collapse of multi-storey buildings due to sudden column loss. Part I: Simplified assessment framework.” *Eng. Struct*. 30(5): 1308–1318.

Kakaletsis, D. J., and C. G. Karayannis. 2009. “Experimental investigation of infilled reinforced concrete frames with openings.” *ACI Struct. J.* 102 (2): 132–141.

Kunnath, S.K., Bao, Y., El-Tawil, S. 2018. “Advances in Computational Simulation of Gravity-Induced Disproportionate Collapse of RC Frame Buildings.” *J. Struct. Eng.* 144(2): 03117003.

Li, S., Kose, M.M., Shan, S., Sezen H. 2019. “Modeling Methods for Collapse Analysis of Reinforced Concrete Frames with Infill Walls.” *J. Struct. Eng.* 145(4): 04019011.

Marchand, K.A., Stevens, D.J. 2015. “Progressive Collapse Criteria and Design Approaches Improvement.” *J. Perform. Constr. Facil.* 29(5): B4015004.

McKenna F.,. Fenves G.L., Scott M.H. 2000. Open system for earthquake engineering simulation. University of California, Berkeley, CA.

Mehrabi, A.B., Shing, P.B. 1997. “Finite element modelling of masonry-infilled RC frames.” *J. Struct. Eng.* 123(5): 604-13.

Mehrabi, A.B., Shing, P.B., Schuller, M.P., Noland, L. 1996. “Experimental Evaluation of Masonry-Infilled RC Frames.” *J. Struct. Eng.* 122(3): 228-237.

Morandi, P., Hak, S., Magenes, G. 2018. “In-plane Experimental Response of Strong Masonry Infills.” *Eng. Struct.* 156: 503-521.

Panagiotakos, T.B., Fardis, M.N. 1996. “Seismic response of infilled RC frames structures.” XXI WCEE, Acapulco, Mexico.

Papia, M., Cavaleri, L., Fossetti, M. 2003. “Infilled frames: developments in the evaluation of the stiffening effect of infills.” *Structural engineering and mechanics* 16(6): 675-93.

Pham X.D., Tan K.H., Yu J. 2015. “A simplified approach to assess progressive collapse resistance.” *Eng. Struct.* 101: 45-57

Pham, A.T., Tan, K.H., Yu, J. 2017. “Numerical investigations on static and dynamic responses of reinforced concrete sub-assemblages under progressive collapse.” *Eng. Struct*. 149: 2–20.

Qian, K. & Li, B. 2017. “Effects of Masonry Infill Wall on the Performance of RC Frames to Resist Progressive Collapse.” *J. Struct. Eng.* 143(9): 04017118.

Ren, P., Li, Y., Lu, X., Guan, H., Zhou, Y. 2016. “Experimental investigation of progressive collapse resistance of one-way reinforced concrete beam–slab substructures under middle-column-removal scenario” *Eng. Struct.* 118: 28–40

Razvi S.R., Saatcioglu M. 1992. “Strength and Ductility of Confined Concrete.” *J. Struct. Eng.* 118(6): 1590-1607.

Shan, S. D., Li S., Xu S. Y., Xie L. L. 2016. “Experimental study on the progressive collapse performance of RC frames with infill walls.” *Eng. Struct.* 111: 80–92.

Stavridis, A., Shing, P.B. 2010. “Finite-Element Modeling of Nonlinear Behavior of Masonry-Infilled RC Frames.” *J. Struct. Eng.* 136(3): 285-296.

Vlassis, A.G., Izzuddin, B.A., Elghazouli, A. Y., Nethercot D.A. 2008. “Progressive collapse of multi-storey buildings due to sudden column loss. Part II: Application.” *Eng. Struct*. 30(5): 1424-1438

Weng, J., Lee, C. K., Tan K. H. & Lim N. S. 2017. “Damage as-sessment for reinforced concrete frames subject to progressive collapse.” *Eng. Struct*. 149: 147–160.

Xavier, F.B., Macorini, L. Izzuddin, M.B. 2015. “Robustness of Multistory Buildings with Masonry Infill.” *J. Perform. Constr. Facil.* 29(5): B4014004.

Xiao, Y., Kunnath, S., Li, F.W., Zhao, Y.B., Lew, H.S., Bao, Y. 2015. “Collapse test of three-story half-scale reinforced concrete frame building.” *ACI Struct. J.* 112(4): 429-438.

Yu, J., Tan, K.H. 2013. “Experimental and numerical investigation on progressive collapse resistance of reinforced concrete beam column subassemblages.” *Eng. Struct.* 55:90–106.

TABLES

Table 1. Experimental and numerical specimens and test set-up details.

Author	Specimen code	Type	Sotrey no.	Bays no.	Scale	Masonry type	Lateral constraint	Seismic detailing	Aspect ratio (l_b/h_c)
Li et al. (2019)	(no code)		1	2	1/3	Brick	two-sides (partial)	Yes	1.58
Qian and Li (2017)	WSS	Experimental	2	1	1/4	Brick	one-side (full)	Yes	2.41
Qian and Li (2017)	WNL		2	1	1/4	Brick	one-side (full)	No	3.28
	FEM-S1F-B500						no	Yes	1.02
	FEM-S1R-B500						two-sides (full)	Yes	1.02
	FEM-nS1F-B500						no	No	1.02
	FEM-nS1R-						two-sides (full)	No	1.02
Di Trapani et al. (2020a)	FEM-S2R-B500	Numerical	1	1	1/1	Clay hollow	two-sides (full)	Yes	2.04
	FEM-nS2F-B500						no	No	2.04
	FEM-nS2F-B200						no	No	1.83
	FEM-nS2F-B300						no	No	1.90
	FEM-nS2R-						two-sides (full)	No	1.90

Table 2. Geometric and mechanical details of experimental and numerical specimens and parameters for the identification of the equivalent strut width of S1 struts

Specimen reference	t	h_c	h_c'	l_b	l_b'	d	b_{wc}	h_{wc}	b_{wb}	h_{wb}	E_{m2}	E_{m1}	$\tilde{E}_m$	E_c	λ^*	w
	(mm)	(mm)	(mm)	(mm)	(mm)	(mm)	(mm)	(mm)	(mm)	(mm)	(MPa)	(MPa)	(MPa)	(MPa)	-	(mm)
Li et al. (2019)	63.5	950	1100	1500	1700	2025	200	200	100	150	5376	7680	6426	35725	3.170	274.5
Qian and Li (2017) - WSS	65	685	825	1650	1800	1980	150	150	90	140	4410	6300	5271	32837	7.191	156.1
Qian and Li (2017) - WNL	65	685	825	2250	2400	2538	150	150	90	140	4410	6300	5271	32837	16.915	129.4
FEM-S1F-B500	300	2670	3170	2720	3440	4678	720	300	300	500	6401	5032	5675	31476	1.659	1080.8
FEM-S1R-B500	300	2670	3170	2720	3440	4678	720	300	300	500	6401	5032	5675	31476	1.659	1080.8
FEM-nS1F-B500	300	2670	3170	2720	3440	4678	720	300	300	500	6401	5032	5675	31476	1.659	1080.8
FEM-nS1R-B500	300	2670	3170	2720	3440	4678	720	300	300	500	6401	5032	5675	31476	1.659	1080.8
FEM-S2R-B500	300	2670	3170	5440	6160	6928	720	300	300	500	6401	5032	5675	31476	8.587	629.0
FEM-nS2F-B500	300	2670	3170	5440	6160	6928	720	300	300	500	6401	5032	5675	31476	8.587	629.0
FEM-nS2F-B200	300	2970	3170	5440	6160	6928	720	300	1000	200	6401	5032	5675	31476	6.490	729.0
FEM-nS2F-B300	300	2870	3170	5440	6160	6928	720	300	700	300	6401	5032	5675	31476	6.190	709.4
FEM-nS2R-B300	300	2870	3170	5440	6160	6928	720	300	700	300	6401	5032	5675	31476	6.190	709.4

Table 3. Masonry infill material properties and parameters for the determination of the nominal stress-strain response of S1 struts

Specimen reference	f_{vm}	f_{m2}	f_{m1}	$\tilde{f}_m$	α	β	γ	δ	f_{md0}	f_{mdu}	ε_{md0}	ε_{mdu}
	(MPa)	(MPa)	(MPa)	(MPa)	-	-	-	-	(MPa)	(MPa)	-	-
Li et al. (2019)	1.08	8.96	12.8	10.71	2.47E+06	4.08	0.00390	0.003823	4.22	0.49	0.000662	0.00803
Qian and Li (2017) - WSS	1.10	7.35	10.5	8.78	1.25E+06	2.52	0.00271	0.003237	4.21	0.42	0.000583	0.00859
Qian and Li (2017) - WNL	1.10	7.35	10.5	8.78	1.19E+06	1.65	0.00366	0.003594	4.27	0.43	0.000647	0.00844
FEM-S1F-B500	1.07	4.18	8.66	6.02	1.07E+07	16.77	0.05008	0.009042	1.56	1.03	0.001605	0.00713
FEM-S1R-B500	1.07	4.18	8.66	6.02	1.07E+07	16.77	0.05008	0.009042	1.56	1.03	0.001605	0.00713
FEM-nS1F-B500	1.07	4.18	8.66	6.02	1.07E+07	16.77	0.05008	0.009042	1.56	1.03	0.001605	0.00713
FEM-nS1R-B500	1.07	4.18	8.66	6.02	1.07E+07	16.77	0.05008	0.009042	1.56	1.03	0.001605	0.00713
FEM-S2R-B500	1.07	4.18	8.66	6.02	8.93E+06	6.83	0.00658	0.004471	1.64	0.38	0.000794	0.00802
FEM-nS2F-B500	1.07	4.18	8.66	6.02	8.93E+06	6.83	0.00658	0.004471	1.64	0.38	0.000794	0.00802
FEM-nS2F-B200	1.07	4.18	8.66	6.02	9.84E+06	7.76	0.00878	0.004942	1.59	0.44	0.000877	0.00789
FEM-nS2F-B300	1.07	4.18	8.66	6.02	1.00E+07	7.53	0.00811	0.004808	1.59	0.42	0.000853	0.00792
FEM-nS2R-B300	1.07	4.18	8.66	6.02	1.00E+07	7.53	0.00811	0.004808	1.59	0.42	0.000853	0.00792

Table 4. Parameters after the calibration α_b and ξ and resulting dimensional properties.

Specimen reference	α_b	ξ	$\alpha_b \cdot l_b$	$\tilde{f}_{md0} = \xi \cdot f_{md0}$	$\tilde{f}_{mdu} = \xi \cdot f_{mdu}$
	-	-	(mm)	(MPa)	(MPa)
Li et al. (2019)	0.500	1	750	4.22	0.49
Qian and Li (2017) - WSS	0.200	0.75	330	3.16	0.32
Qian and Li (2017) - WNL	0.500	0.85	1125	3.63	0.36
FEM-S1F-B500	0.250	0.90	680	1.40	0.93
FEM-S1R-B500	0.200	1.00	544	1.56	1.03
FEM-nS1F-B500	0.500	0.85	1360	1.32	0.87
FEM-nS1R-B500	0.300	1.00	816	1.56	1.03
FEM-S2R-B500	0.200	0.60	1088	0.98	0.23
FEM-nS2F-B500	0.200	0.50	1088	0.82	0.19
FEM-nS2F-B200	0.200	0.25	1088	0.40	0.11
FEM-nS2F-B300	0.150	0.25	816	0.40	0.10
FEM-nS2R-B300	0.150	0.40	816	0.63	0.17

Table 5. Parameters κ and ρ and associated data for their determination.

Specimen reference	K_f	K_s	κ	N_{bmax}	R_f	R_s	ρ	θ
	(kN/m)	(kN/m)	-	(kN)	(kN)	(kN)	-	(°)
Li et al. (2019)	10717.5	45079.7	0.94	34.51	39.70	79.86	0.50	32.91
Qian and Li (2017) - WSS	8123.5	36781.2	0.97	17.31	67.03	58.13	1.15	27.00
Qian and Li (2017) - WNL	3203.7	22151.3	0.74	9.82	26.61	51.56	0.52	25.00
FEM-S1F-B500	117309.0	266586.3	1.05	80.53	478.24	615.59	0.78	42.66
FEM-S1R-B500	234618.0	533172.5	1.05	1084.00	977.65	683.99	1.43	42.66
FEM-nS1F-B500	117309.0	266586.3	1.05	35.00	214.12	581.39	0.37	42.66
FEM-nS1R-B500	234618.0	533172.5	1.05	943.00	697.06	683.99	1.02	42.66
FEM-S2R-B500	29327.3	141476.0	0.70	871.00	453.42	169.68	2.67	27.23
FEM-nS2F-B500	14663.6	70738.0	0.70	104.18	218.80	141.40	1.55	27.23
FEM-nS2F-B200	3128.2	81981.7	0.12	41.61	164.46	79.68	2.06	27.23
FEM-nS2F-B300	7390.5	79771.9	0.30	84.92	222.35	77.17	2.88	27.23
FEM-nS2R-B300	14780.9	159543.8	0.30	1040.00	375.07	123.48	3.04	27.23

Table 6. Experimental and numerical blind test specimens and test set-up details.

Author	**Specimen code**	**Type**	**Storey no.**	**Bays no.**	**Scale**	**Masonry type**	**Lateral constraint**	**Seismic detailing**	**Aspect ratio (l_b/h_c)**
Qian and Li (2017)	WNS	Experimental	2	1	1/4	Brick	one-side (full)	No	2.41
Di Trapani et al. (2020a)	FEM-S2F-B500	Numerical	1	1	1/1	Clay hollow	no	Yes	2.04
	FEM-nS2R-B500						two-sides (full)	No	2.04
	FEM-nS2R-B200						two-sides (full)	No	1.83

Table 7 Geometric and mechanical details of experimental and numerical blind test specimens and parameters for the identification of the equivalent strut width of S1 struts

Specimen reference	t	h_c	h_c'	l_b	l_b'	d	b_{wc}	h_{wc}	b_{wb}	h_{wb}	E_{m2}	E_{m1}	$\tilde{E}_m$	E_c	λ^*	w
	(mm)	(mm)	(mm)	(mm)	(mm)	(mm)	(mm)	(mm)	(mm)	(mm)	(MPa)	(MPa)	(MPa)	(MPa)	-	(mm)
Qian and Li (2017) - WNS	65	685	825	1650	1800	1980	150	150	90	140	4410	6300	5271	32837	7.191	156.1
FEM-S2F-B500	300	2670	3170	5440	6160	6928	720	300	300	500	6401	5032	5675	31476	8.587	629.0
FEM-nS2R-B500	300	2670	3170	5440	6160	6928	720	300	300	500	6401	5032	5675	31476	8.587	629.0
FEM-nS2R-B200	300	2970	3170	5440	6160	6928	720	300	1000	200	6401	5032	5675	31476	6.490	729.0

Table 8. Masonry infill material properties and parameters for the determination of the nominal stress-strain response of S1 struts for the blind test specimens.

Specimen reference	f_{vm} (MPa)	f_{m2} (MPa)	f_{m1} (MPa)	$\tilde{f}_m$ (MPa)	α -	β -	γ -	δ -	f_{md0} (MPa)	f_{mdu} (MPa)	ε_{md0} -	ε_{mdu} -
Qian and Li (2017) - WNS	1.1	7.35	10.5	8.78	1.25E+06	2.52	0.00271	0.003237	4.21	0.42	0.000583	0.00859
FEM-S2F-B500	1.07	4.18	8.66	6.02	8.93E+06	6.83	0.00658	0.004471	1.64	0.38	0.000794	0.008018
FEM-nS2R-B500	1.07	4.18	8.66	6.02	8.93E+06	6.83	0.00658	0.004471	1.64	0.38	0.000794	0.008018
FEM-nS2R-B200	1.07	4.18	8.66	6.02	9.84E+06	7.76	0.00878	0.004942	1.59	0.44	0.000877	0.007885

Table 9. Parameters κ and ρ and associated data for their determination.

Specimen reference	K_f (kN/m)	K_s (kN/m)	κ -	$\nu_{b,max}$ -	$N_{b,max}$ (kN)	R_f (kN)	R_s (kN)	ρ -	θ (°)
Qian and Li (2017) - WNS	8123	39377	0.90	0.034	14.36	38.40	66.38	0.58	29.08
FEM-S2F-B500	14663	70738	0.70	0.036	135.33	256.91	164.02	1.57	27.23
FEM-nS2R-B500	29327	141476	0.70	0.20	757.41	396.03	164.02	2.41	27.23
FEM-nS2R-B200	6256	163963	0.12	0.11	547.79	215.66	79.68	2.71	27.23

Table 10. Parameters α_b and ξ and resulting dimensional properties.

Specimen reference	α_b -	ξ -	$\alpha_b \cdot l_b$ (mm)	$\tilde{f}_{md0} = \xi \cdot f_{md0}$ (MPa)	$\tilde{f}_{mdu} = \xi \cdot f_{mdu}$ (MPa)
Qian et al. (2017) - WNS	0.42	0.800	693	3.37	0.34
FEM-S2F-B500	0.19	0.580	1033.6	0.95	0.22
FEM-nS2R-B500	0.20	0.580	1088	0.95	0.22
FEM-nS2R-B200	0.18	0.250	979.2	0.40	0.11

Table 11. Geometric and mechanical properties of the infilled frames of the sample strut.

t (mm)	h_c (mm)	h_c' (mm)	l_b (mm)	l_b' (mm)	d (mm)	b_{wc} (mm)	h_{wc} (mm)	b_{wb} (mm)	h_{wb} (mm)	E_{m2} (MPa)	E_{m1} (MPa)	$\tilde{E}_m$ (MPa)	f_{vm} (MPa)	f_{m2} (MPa)	f_{m1} (MPa)	$\tilde{f}_m$ (MPa)
300	2900	3400	5900	6300	7159	400	800	300	500	6401	5032	5675	1.07	8.66	4.18	6.02

Table 12. Reinforcement details for the central span beams.

Section	Stories 1-2-3 Top reinforcement	Stories 1-2-3 Bottom reinforcement	Stories 4-5-6 Top reinforcement	Stories 4-5-6 Bottom reinforcement
1-1	7 ϕ 16	4ϕ16	6 ϕ 16	3ϕ16
2-2	7 ϕ 16	4ϕ16	6 ϕ 16	3ϕ16

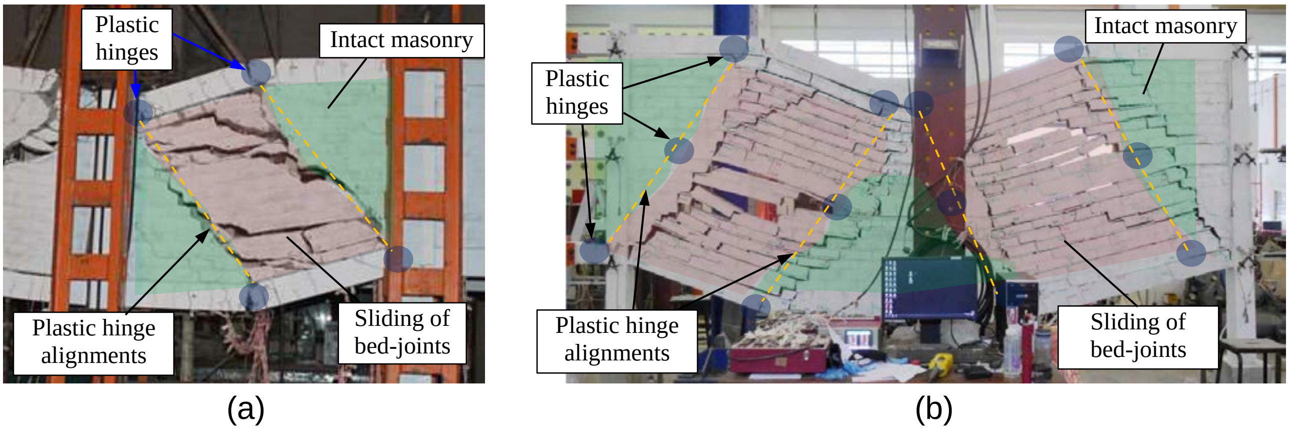

Fig. 1. Interpretation of the damage mechanism in pushdown tests of infilled frames: a) One-story infilled frame (**Li et al. 2019**); b) Two-story infilled frame (**Qian and Li 2017**).

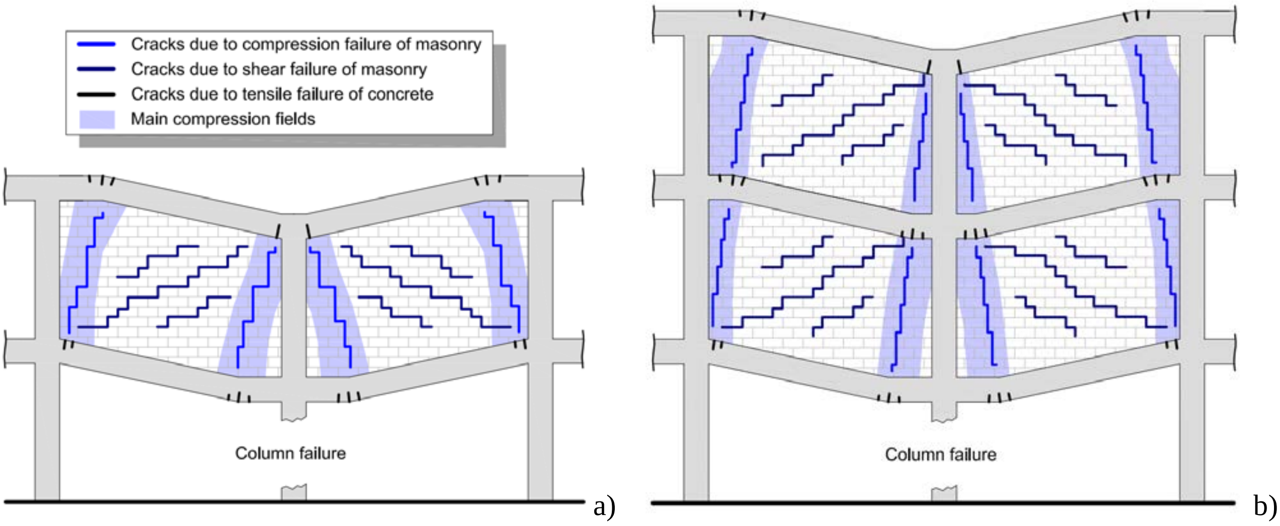

Fig. 2. Typical damage mechanisms associated with progressive collapse of infilled frames: a) One-story infilled frames; b) Multi-story infilled frames.

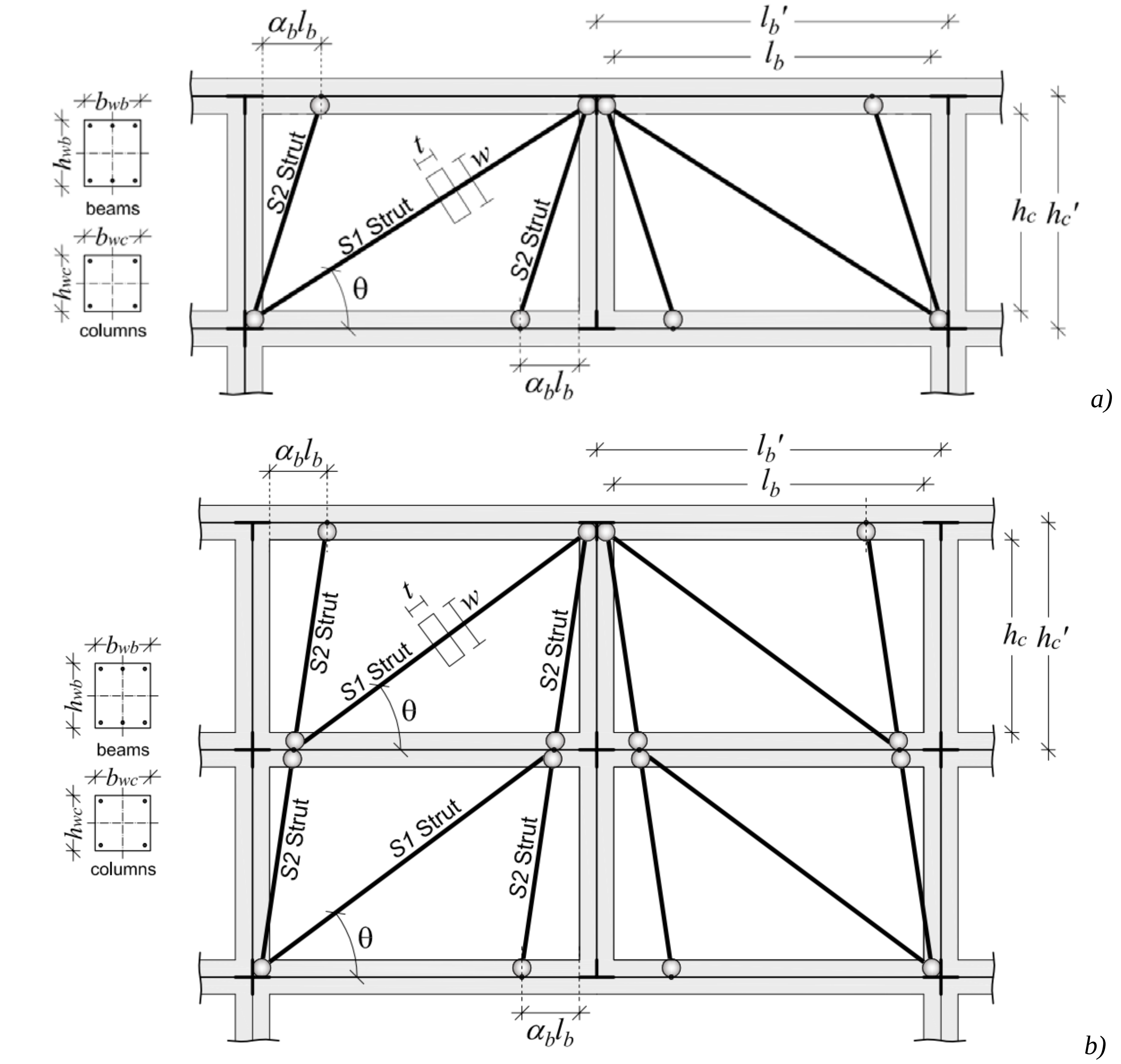

Fig. 3. Proposed equivalent strut model for: a) One-storey infilled frames; b) Multi-story infilled frames.

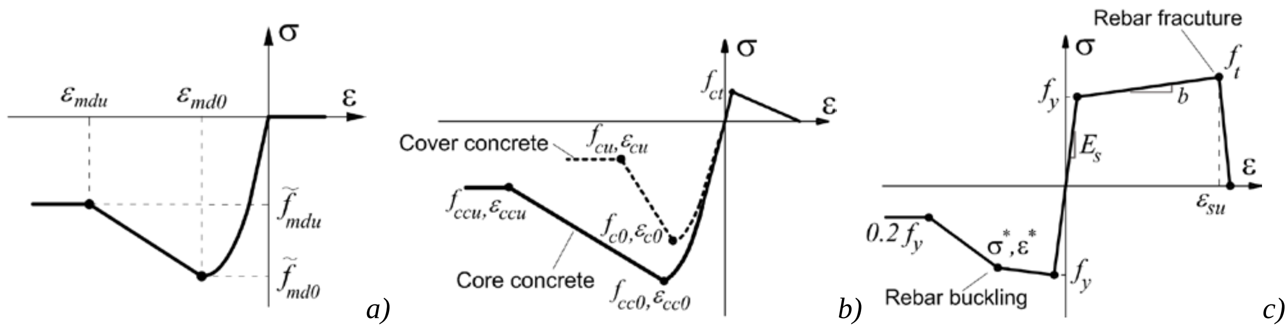

Fig. 4. Adopted stress-strain model for: a) S1 struts; b) Confined and unconfined concrete; c) Rebars.

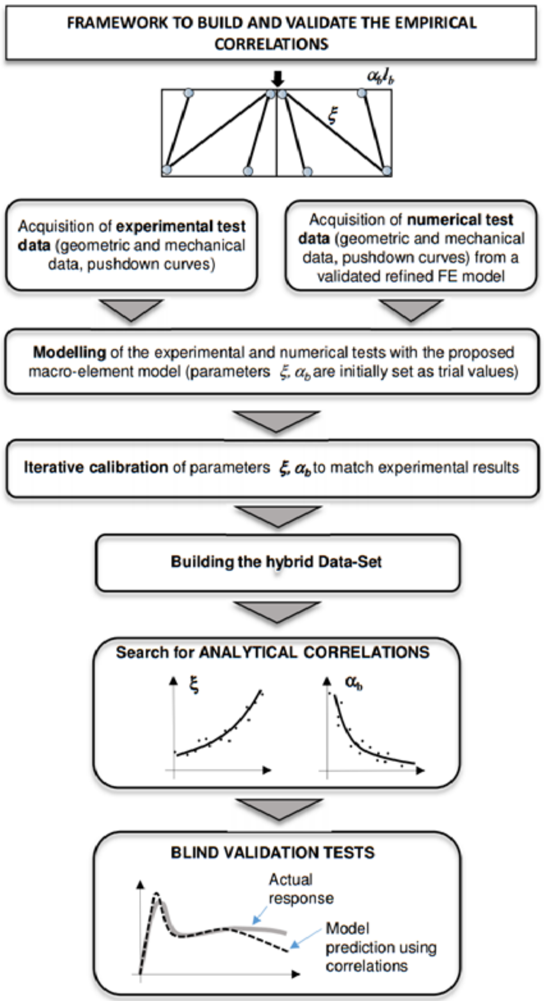

Figure 5: Framework to build and validate the empirical correlations.

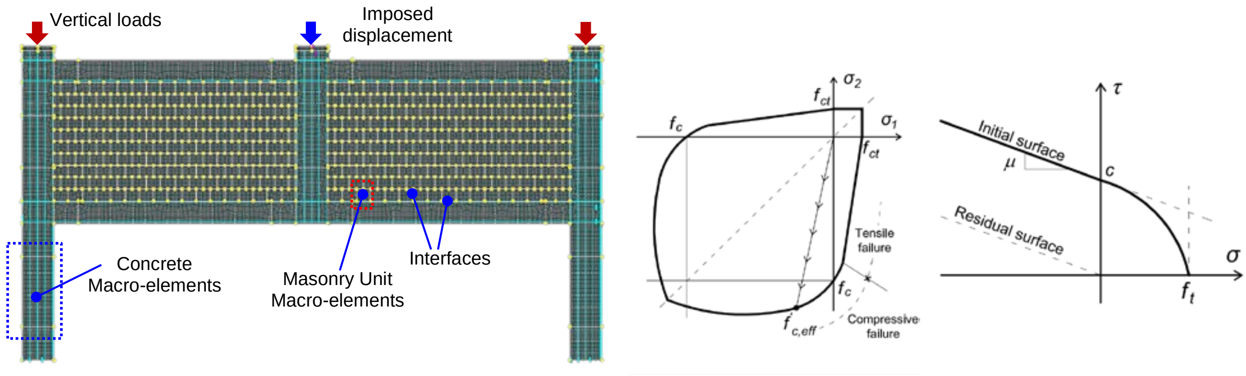

(a) (b) (c)

Figure 6: Refined FE model (Di Trapani et al. 2020): a) Overall assembly of the model; b) Concrete and masonry macro-elements failure surface; c) interfaces failure surface.

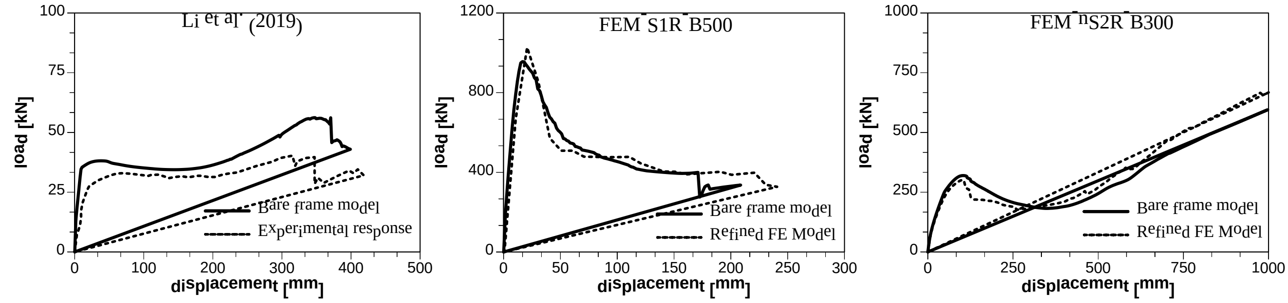

Fig. 7. Bare frame experimental and numerical pushdown curves and model predictions.

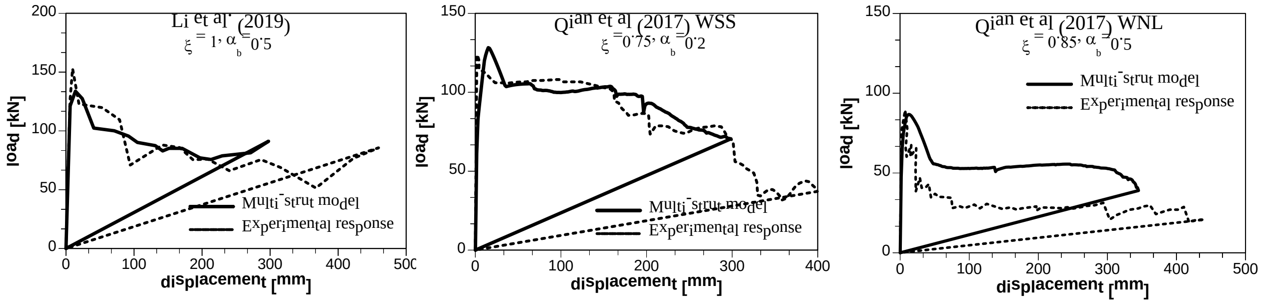

Fig. 8. Experimental pushdown curves and proposed model pushdown curves at the end of the calibration.

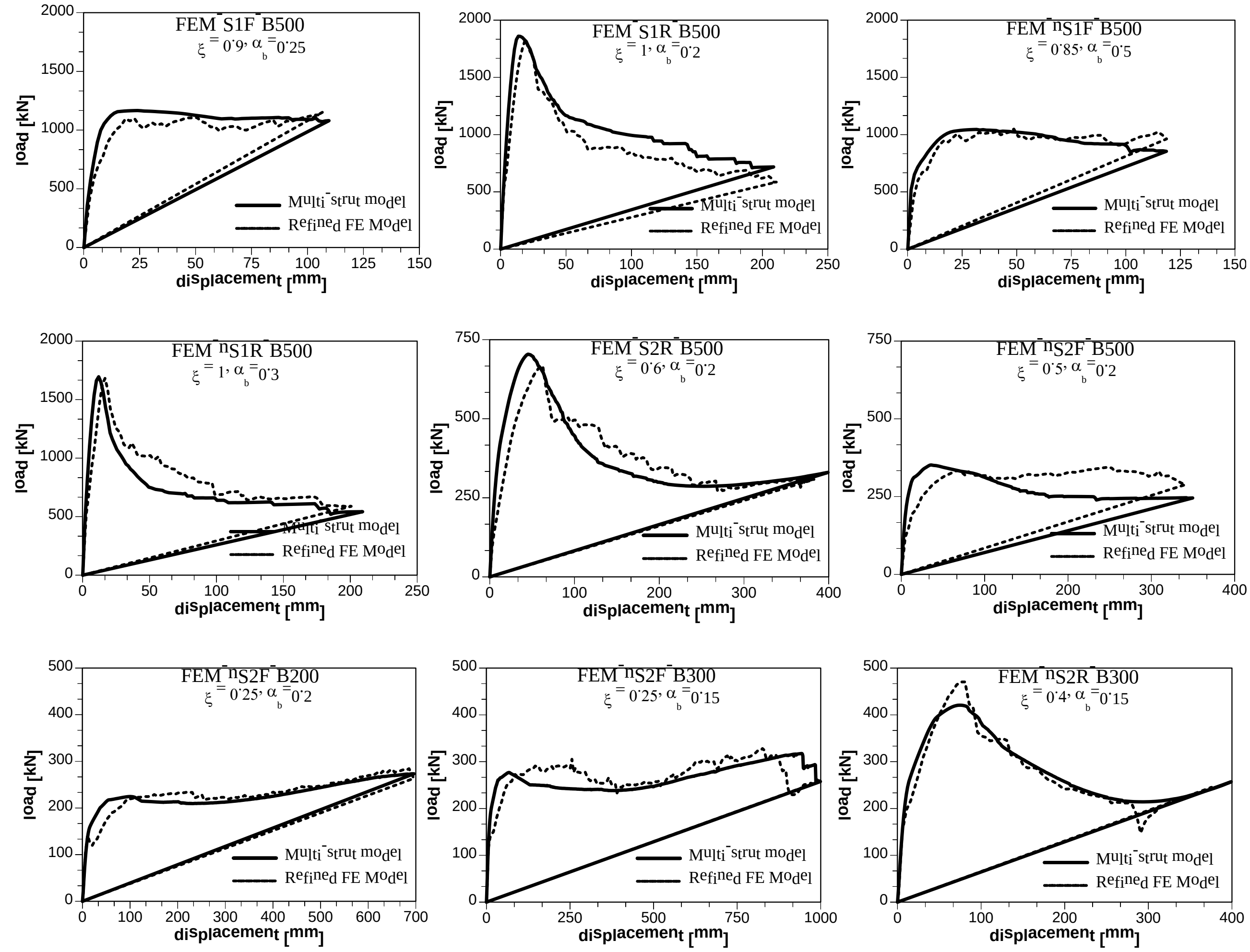

Fig. 9. Numerical pushdown curves from the refined FE model and proposed model pushdown curves at the end of the calibration.

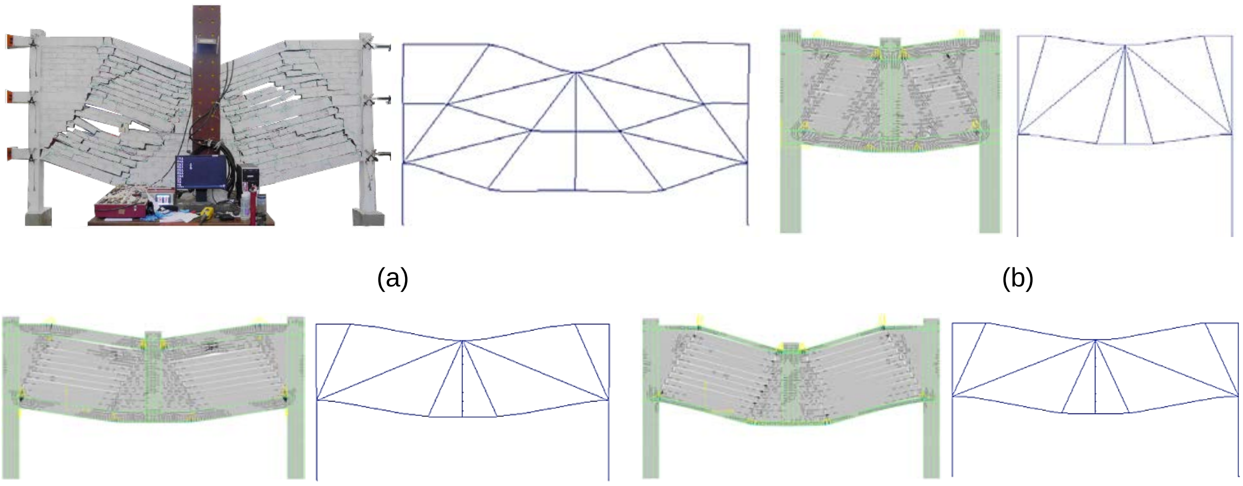

Fig. 10. Comparison between the deformed shapes of experimental and numerical specimens and those obtained after the equivalents strut models calibration: a) Qian and Li (2017) – WNL; b) FEM-S1R-B500; c) FEM-S2R-B500; d) FEM-nS2F-B200

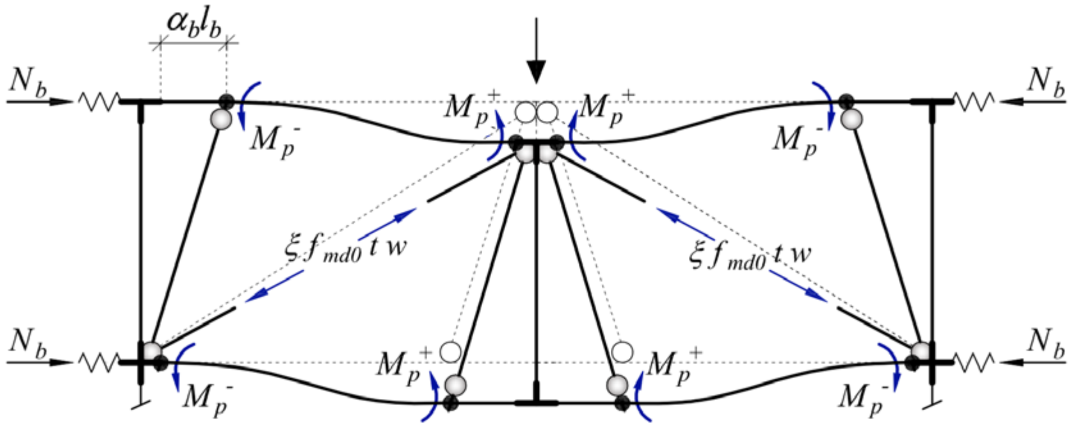

Fig. 11. Typical collapse mechanism of the proposed equivalent strut model (sample for a one-storey infilled frame).

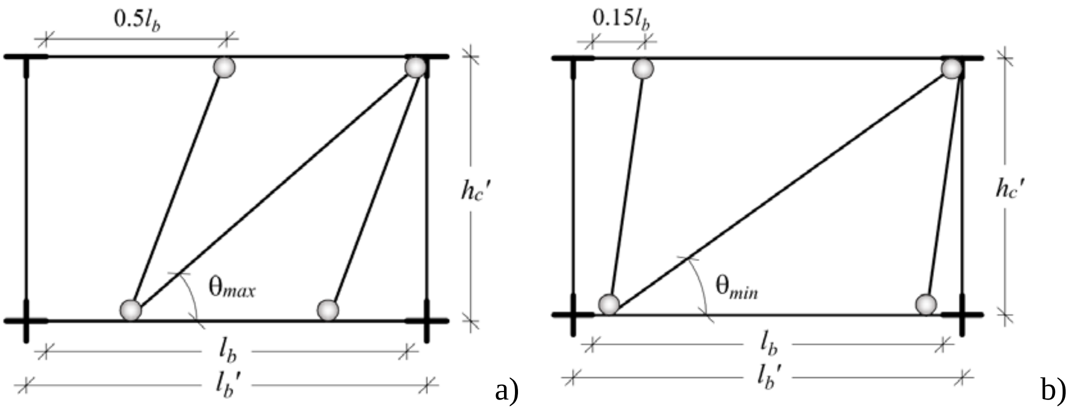

Fig. 12. Limit configurations of the equivalent strut model for the estimation of the average angle of inclination of S1 strut in multi-storey infilled frames: a) θ_{max} configuration; b) θ_{min} configuration.

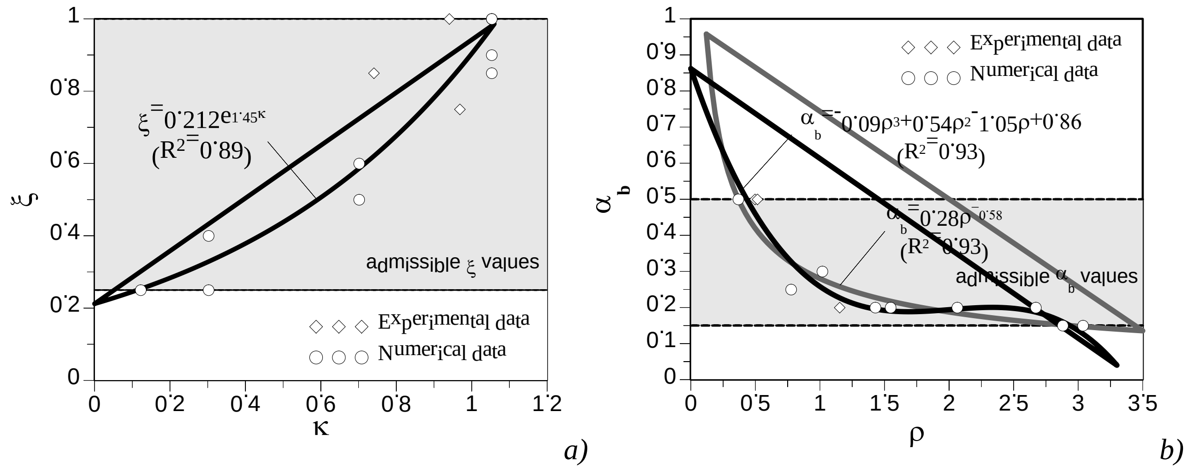

Fig. 13. Experimental and numerical data and analytical correlations: a) ξ–κ; b) α_b–ρ.

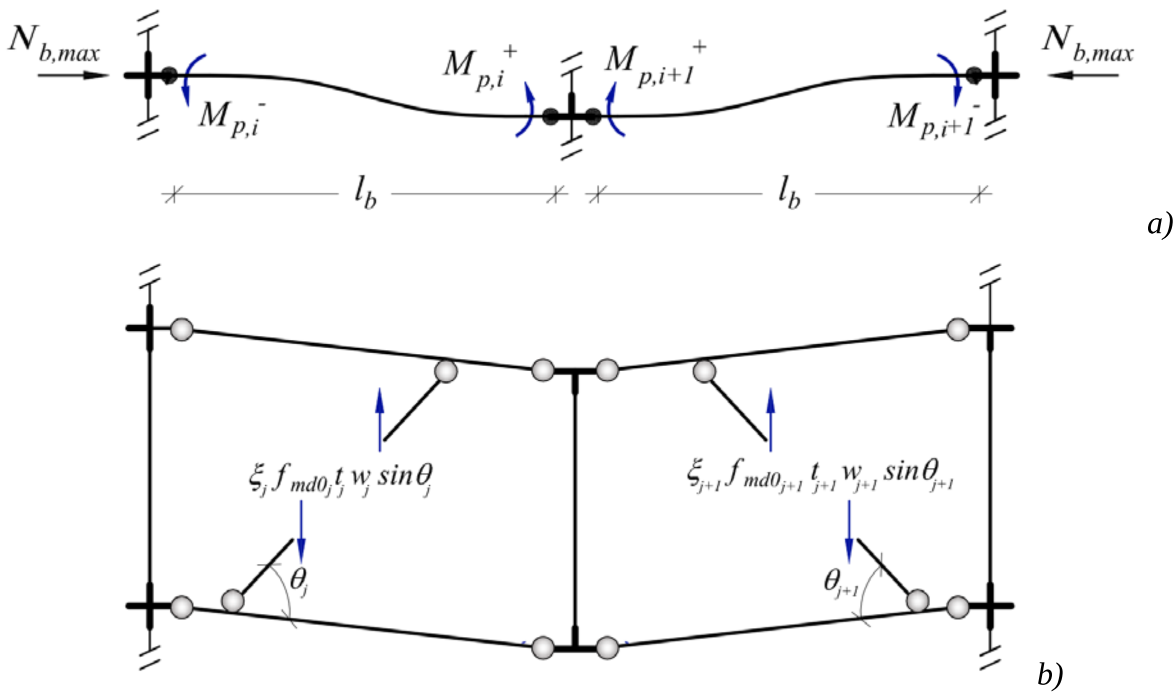

Fig. 14. Simplified limit equilibrium schemes for the evaluation of: a) R_f ; b) R_s.

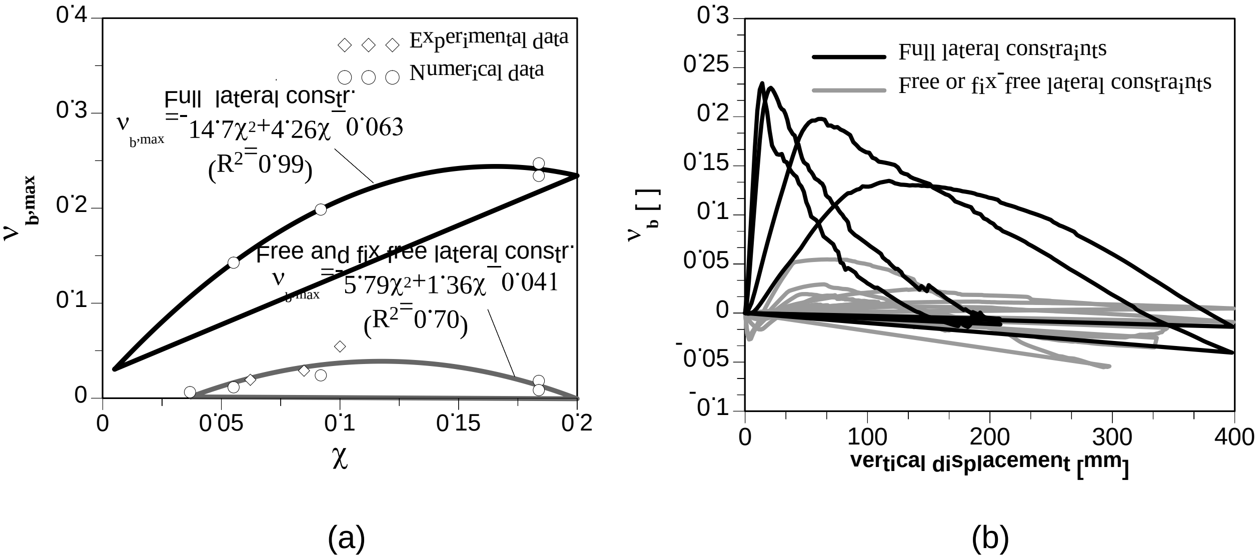

Fig. 15. Average dimensionless axial forces in beams: a) experimental and numerical data and analytical correlations with the and the height-to-length ratio (χ) for different lateral restraint conditions; b) variation with the vertical displacement.

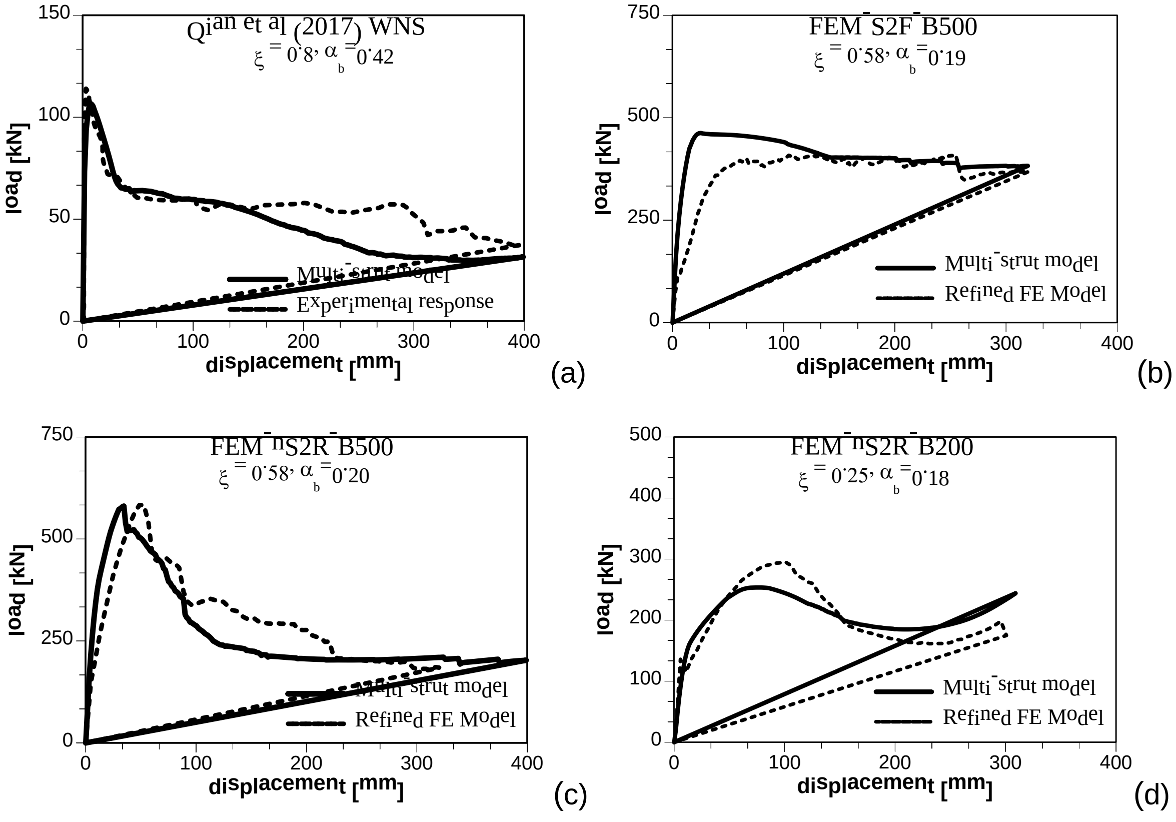

Figure 16. Blind validation tests of the proposed model with experimental and numerical test results.

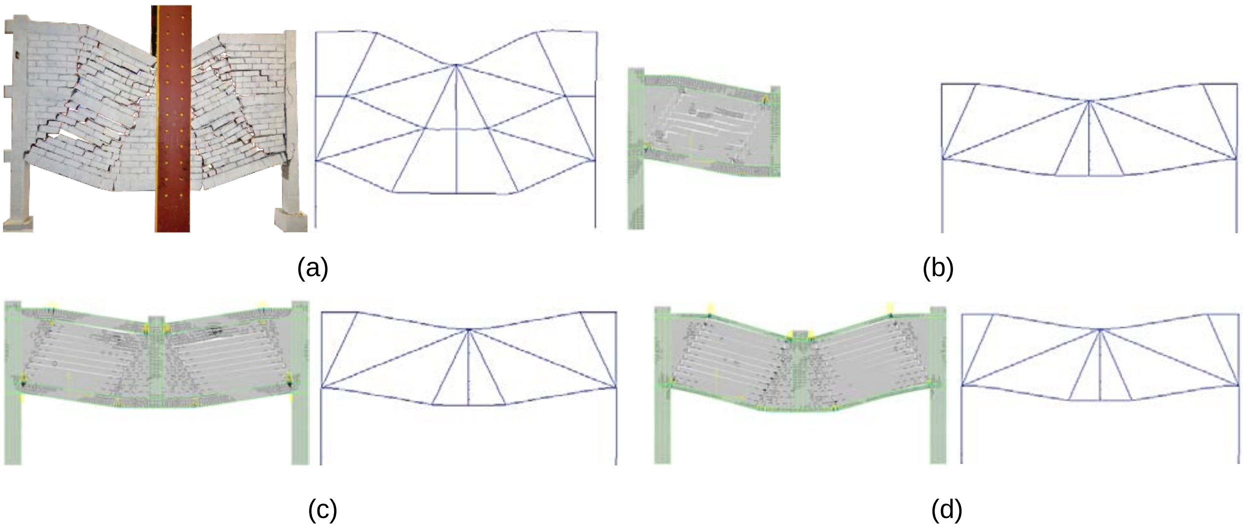

Fig. 17. Comparison between the deformed shapes of experimental and numerical blind test specimens and those predicted by te model: a) Qian and Li (2017) – WNS; b) FEM-S2F-B500; c) FEM-nS2R-B500; d) FEM-nS2R-B200

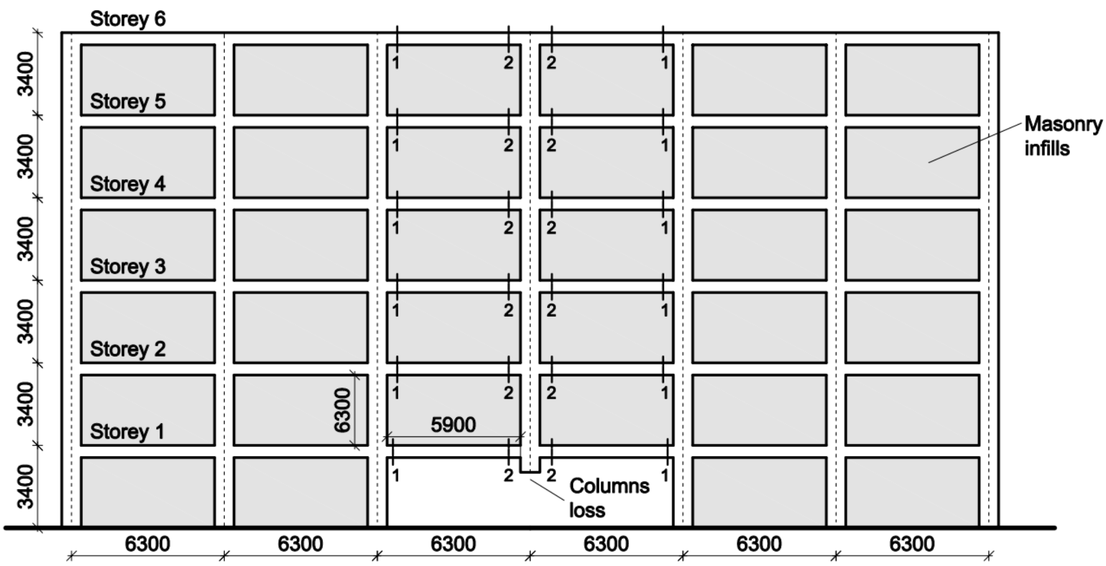

Fig. 18. Sample structure geometry (dimensions in mm).

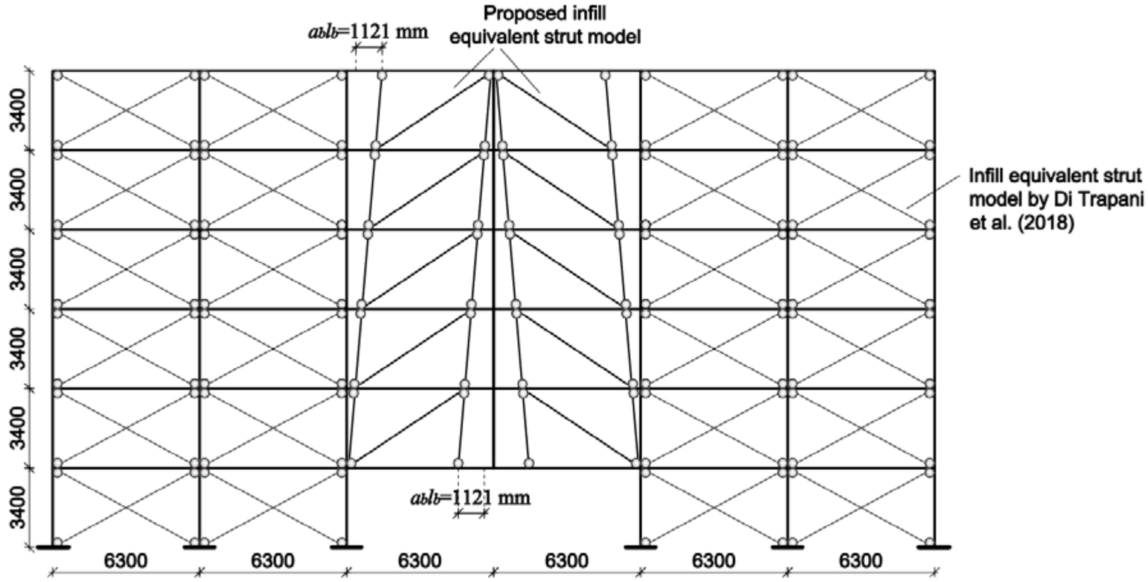

Fig. 19. Sample structure multi-strut progressive collapse model (dimensions in mm).

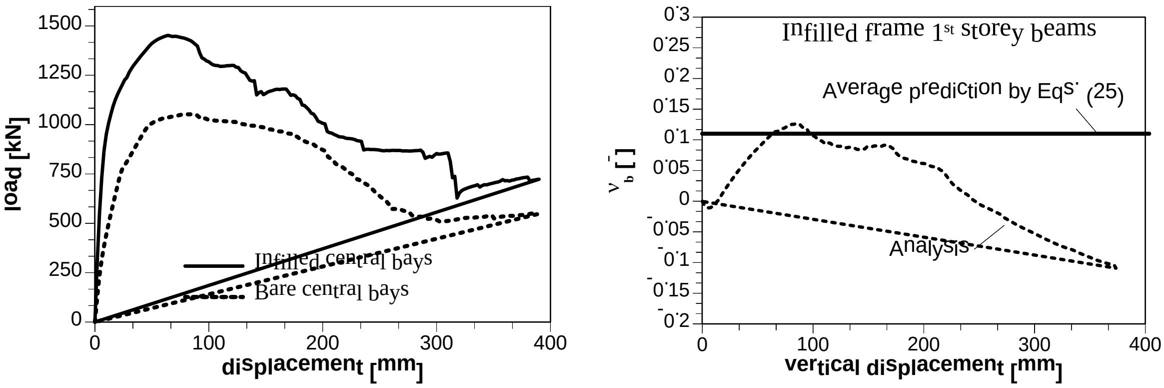

(a) (b)

Fig. 20. Results of the pushdown tests: a) comparison between pushdown responses of the model with and without infills in the central bays; b) Dimensionless axial force in first storey beams for the model with the infills in the central bays.

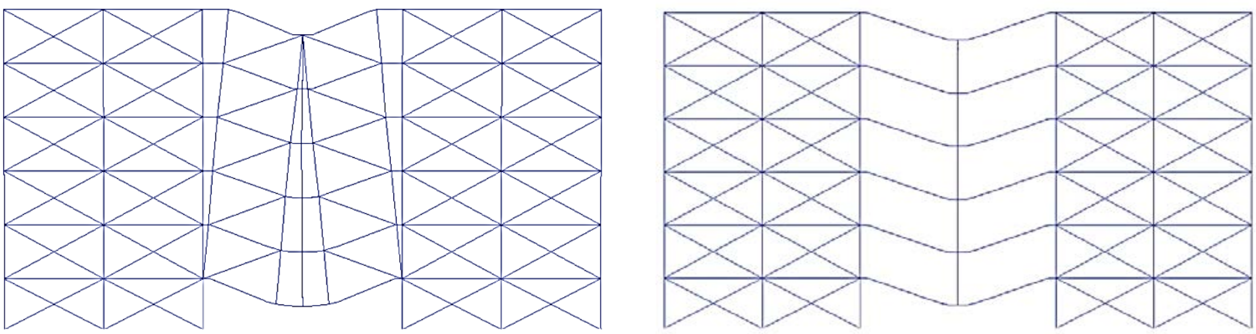

(a) (b)

Fig. 21. Deformed shapes of the models during the pushdown tests: a) Infilled central bays; b) Bare central bays.